A Qutrit in Ultracold Rubidium-87

by

Joseph Lindon

A thesis submitted in partial fulfillment of the requirements for the degree of

Master of Science

Department of Physics

University of Alberta

Abstract

Most quantum computers are based on elements with many addressable states, yet restrict themselves to a two-level subset, a qubit. In principle, more states could be used in each element to form a d-dimensional qudit, increasing the Hilbert space dimension and thus the computational power of the device. A qutrit is a three-level qudit, and is a natural first step to working with more dimensions.

Universal quantum computers require arbitrary single-qudit unitary gates with high fidelity of control. Commonly, there are some couplings between levels that are more difficult to control in a quantum system than others, for example, if they are forbidden transitions by dipole selection rules, if they have a resonance frequency far off from the other transitions, or if the coupling is degenerate with another coupling and thus cannot be controlled in isolation.

In this work, we demonstrate full unitary control on an ensemble qutrit of ultracold ^{87}Rb. We also demonstrate a method for performing rotations between levels which are not otherwise convenient to couple because of degeneracies. We perform the quantum Fourier transform on the qutrit with and without the synthesized coupling and find similar final state fidelities with each method. The dominant error mechanism causes loss of purity in the qutrit, and our analysis suggests this may be caused by inhomogeneity in the dipole trap.

Our work is directly applicable to more conventional quantum platforms,

including superconducting qubits, trapped-ion qubits, and neutral single-atom qubits.

Preface

Chapter 4 of this thesis was published in *Physical Review Applied* under the title "Complete unitary qutrit control in ultracold atoms". I wrote it together with my co-authors Dr. Arina Tashchilina, Dr. Logan W. Cooke, and Dr. Lindsay J. LeBlanc. While I was primarily responsible for the project, A. Tashchilina and L. Cooke contributed to data collection, frequently worked with me to maintain, repair and operate the apparatus, helped to edit the manuscript, and provided supervision. L. LeBlanc contributed to figure production, manuscript writing and editing, and provided guidance and supervision throughout.

The core apparatus was assembled and fully operational before I joined the group. It is the product of work by Dr. LeBlanc, Taras Hrushevskyi, and many others. Its design and construction is well documented in Taras' thesis [37].

Acknowledgements

First I would like to thank Dr. Lindsay J. LeBlanc. You are an incredible supervisor, and have created a group with both interesting research and a great atmosphere. I am very grateful for the opportunity to learn and work with your group. Thank you as well for your career advice and for your encouragement to finish this document!

Thank you to the other members of my committee, Dr. Frank Hegmann and Dr. Igor Boettcher, for your guidance, and to Dr. Barry Sanders, who met with my collaborators and I to advise us on the qutrit project.

When I came to Edmonton in June 2020, I had no background in atomic physics. Almost everything I know is thanks to Dr. Arina Tashchilina and Dr. Logan W. Cooke. I am so thankful that you were around to guide me and to teach me. You are both incredibly patient, friendly, and knowledgeable, and I am very glad we worked together.

Thank you to NSERC for their financial support through the CGS M program.

Finally I'd like to thank my friends and family for all of their support throughout my degree. Special thanks to my mom and grandpa for helping me practice my defence. Sheila, thank you for your constant support, understanding, and for learning what a qubit is for me.

Contents

List of Tables

List of Figures

List of Symbols

a, b, c Population amplitude in states $|0\rangle$, $|1\rangle$, $|2\rangle$

ϕ Complex phase. In a qubit, the relative phase between states $|0\rangle$ and $|1\rangle$. In a qutrit, ϕ_1 is the relative phase between $|0\rangle$ and $|1\rangle$, and ϕ_2 is the relative phase between $|0\rangle$ and $|2\rangle$

θ Zenith angle for visualization of a qubit on the Bloch sphere, $\theta = \arccos a$

χ Angular displacement about the rotation axis $\hat{\Omega}$ for some unitary operation $\hat{U}$

φ Phase of a rotation $\hat{U}$

$\hat{U}$ Arbitrary unitary rotation. $\hat{U}^{\mathrm{I}}$ is a single-tone decomposition of the unitary transform, $\hat{U}^{\mathrm{II}}$ is a dual-tone operator decomposition. $\hat{U}_\theta(\eta, \epsilon)$ is a virtual phase gate

$|b\rangle$ Classical bit state, either 0 or 1

$\mathbb{Z}/2$ The set of integers modulo 2, i.e. 0 and 1

Ω Rabi frequency

$|\psi\rangle$ Quantum state, described as a ket

$\hat{\rho}$ Density matrix operator

$\hat{\sigma}_x, \hat{\sigma}_y, \hat{\sigma}_z$ Pauli matrices

$\hat{\lambda}_k$ Gell-Mann matrices

S Electron spin

I Nuclear spin

L Electron orbital angular momentum

F Total atomic angular momentum

ΔE_{HF} Ground-state hyperfine splitting, equivalent to $\hbar\omega_0$

μ Magnetic dipole moment

d Electric dipole operator

$\mathbf{B}$ Magnetic flux density

B_0 Bias magnetic flux density, providing Zeeman splitting

$\mathcal{E}$ Electric field

ω Angular frequency. ω_0 is the resonant frequency for the ground-state hyperfine splitting in the absence of a Zeeman splitting, equivalent to $\Delta E_{\mathrm{HF}}/\hbar$. ω_Z is the resonant frequency for the Zeeman splitting, ω_X is the resonant frequency for coupling X. ω without additional subscripts or superscripts is the frequency of a transition-driving magnetic field

Δ Detuning between a driving frequency and the resonance frequency

$\mathbf{X}$ One of the qutrit couplings: A which couples $|0\rangle$ and $|1\rangle$, B which couples $|1\rangle$ and $|2\rangle$, or C which couples $|0\rangle$ and $|2\rangle$

m_F Magnetic sub-level of hyperfine state F.

λ Dimensionless parameter used in perturbation theory, set to 0 for no perturbation, and to 1 when the perturbation is applied

$\hat{H}$ Hamiltonian of a quantum system. When considering the Zeeman effect, $\hat{H}_0$ is the atomic Hamiltonian excluding the effect, and $\hat{H}_Z$ is a Zeeman term. $\hat{H}_{\mathcal{E}}$ is a term associated with the Stark shift. $\hat{H}_{\mathrm{at.}}$ is a diagonalized Hamiltonian, truncated to the three qutrit levels. H_I is an interaction term associated with a perturbing oscillating magnetic field. $\hat{\tilde{H}}$ is a Hamiltonian in a rotating frame, $\hat{W}$

α Polarizability, α_0 is the static polarizability, and α_2^F is the tensor polarizability of hyperfine state F

$\hbar$ Reduced Planck constant

$\mathcal{P}$ Purity

$\hat{R}_k$ Readout operator

$\mathbf{F}_{\mathrm{SG}}$ Stern-Gerlach force

$\hat{F}$ Quantum Fourier transform

$\mathcal{F}$ Quantum state fidelity

Chapter 1

Introduction

In the near-century since quantum mechanics was formulated, we have developed a number of technologies that rely on its foundations. Among these are photovoltaics, lasers, and magnetic resonance imaging. Now, a new generation of quantum technologies are being rapidly developed – quantum sensing [23], quantum networking [33], and quantum computing [24].

Most quantum computers are based on controllable two-level quantum systems, *qubits*, but nature frequently provides many more than two levels that a quantum engineer can manipulate. This thesis develops operations on the *qutrit*, a three-level quantum system. The work has been published in *Physical Review Applied* [45].

The qutrit used in this work is based on an ensemble of ultracold ^{87}Rb. Because nature is inherently quantum-mechanical, there are many promising potential platforms in development as quantum computers. While it is unlikely that ensembles of ^{87}Rb or ensembles of any other neutral atom will be the predominant quantum element in future quantum processors, the control techniques can be adapted to single-neutral-atom processors and to higher dimensional qudits on platforms such as trapped ions and superconducting circuits.

Chapter 2

Background

This chapter provides the necessary background to understand the contents of this thesis, assuming an undergraduate-level understanding of quantum mechanics and linear algebra.

We begin with a broad discission of quantum computing (sec. 2.1) and atomic physics (sec. 2.2), then discuss qutrit gates (sec. 2.3) and quantum state tomography (sec. 2.4).

2.1 Quantum Computing

Quantum computing is a very active field, with new and old companies both investing heavily in the technology in the hopes of building practical quantum computers before their competitors. This section will motivate the developments along with the benefits of developing three-level qutrits and higher dimensional quantum elements into quantum information processors.

2.1.1 Motivations

> Why *quantum* information processing? The shortest of answers to this question would be, why not?
>
> David P. DiVincenzo [24]

The classical computers we use today are incredible machines that have transformed virtually every aspect of modern life. They are highly adaptable

and can be applied to almost any task. There are, however, classes of problems that today's computers cannot solve efficiently but quantum computers could. One of these classes are problems that involve simulating fundamentally quantum processes like materials science and chemistry. In principle, quantum computers could be used to design drugs and simulate their interactions with other molecules in the body [16, 40, 66]. They could also help researchers find better chemistries to build batteries [36]. There are a number of other challenges that quantum information processing could solve much more efficiently than any classical processor, such as highly constrained optimization problems which appear in logistics [61] and finance [60].

2.1.2 Qubits

A bit is a unit of information that takes on the discrete values of $|0\rangle$ or $|1\rangle$. In isolation, this abstract concept wouldn't be very useful, but groups of bits are used to represent meaningful ideas like letters, numbers, and instructions for the manipulation of other bits. The only one-bit operations are identity, $\hat{1}|b\rangle = |b\rangle$ and NOT, $\texttt{NOT}|b\rangle = |b+1\rangle$ where $b \in \mathbb{Z}/2$.

A quantum bit (qubit) is a simple two-level quantum system. Like a classical bit, a qubit can take on the discrete values of $|0\rangle$ and $|1\rangle$, but it can also take on any superposition of the two,

$$\begin{aligned} |\psi\rangle &= \alpha|0\rangle + \beta|1\rangle \\ &= ae^{i\phi_a}|0\rangle + be^{i\phi_b}|1\rangle \\ &= e^{i\phi_a}(a|0\rangle + be^{i\phi}|1\rangle) \end{aligned} \tag{2.1}$$

where $a, b, \phi_a, \phi_b, \phi$ are all real numbers, α and β are complex. Like all quantum systems, the global phase (ϕ_a in eq. (2.1)) can be ignored because there is no experiment that could distinguish between states with two different values of ϕ_a. Normalization requires $a^2 + b^2 = 1$, so there are two free parameters: $a \in [0, 1]$ and $\phi \in [0, 2\pi)$. A qubit state can be written as a column vector,

$$|\psi\rangle = \begin{pmatrix} a \\ be^{i\phi} \end{pmatrix}. \tag{2.2}$$

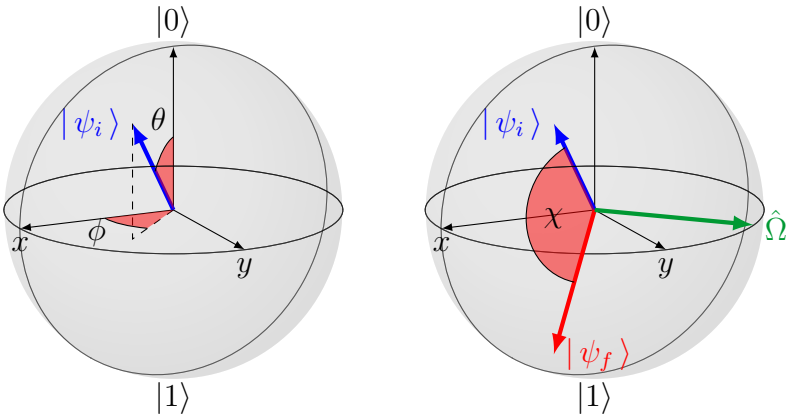

Figure 2.1: (a) The qubit state $|\psi_i\rangle$ drawn on the Bloch sphere with parameters $\theta = \phi = \frac{\pi}{4}$. (b) A rotation about $\hat{\Omega}$ (green) of angle χ brings the state $|\psi_i\rangle$ to state $|\psi_f\rangle$ (red).

It is very useful conceptually to visualize the state of a qubit using the Bloch sphere. Figure 2.1(a) shows the Bloch sphere representation of a qubit state. The zenith angle in the visualization is $\theta = \arccos a$, with the azimuthal angle ϕ, where a and ϕ are as in eq. (2.2).

There are two categories of qubit manipulations – unitary evolutions and projective measurements. Unitary evolution of the qubit's state can be expressed as a matrix $\hat{U}$ in the group SU(2), which means it is unitary ($\hat{U}^{-1} = \hat{U}^\dagger$ for the Hermitian conjugate $\hat{U}^\dagger$), and has determinant 1 (no effect on the global phase). The group SU(2) is generated by exponentiating the three Pauli matrices $\hat{\sigma}_x, \hat{\sigma}_y, \hat{\sigma}_z$. Unitary evolution can be visualized as a rotation around some unit vector $\hat{\Omega}$ on the Bloch sphere, as shown in figure 2.1(b). Unlike unitary evolution which has a fully deterministic result, projective measurement is a probabilistic process. The probability of projecting onto $|\xi\rangle$ is

$$P(|\xi\rangle) = \langle\psi|\xi\rangle\langle\xi|\psi\rangle. \tag{2.3}$$

After a projective measurement, the qubit is no longer in its initial state $|\psi\rangle$, but in one of the eigenstates of $|\xi\rangle\langle\xi|$.

2.1.3 Qutrits

Digital computers use binary logic for good reasons. Electric potential is a continuous variable, and must be sternly wrangled into discrete ranges representing $|0\rangle$ and $|1\rangle$[1]. The electronic complexity of implementing 3-valued or d-valued logic gates would mean very complicated logic gates and would require extremely well-characterized transistors to ensure the logic levels remain valid. Even if a binary circuit requires more elementary logic gates in its implementation than a ternary version would, the net benefit of building on boolean logic for digital computers is undisputed.

Similar to their ubiquitous digital counterparts, most gate-based quantum computing platforms are based on two-level qubits. Unlike digital computers though, it is not inherently clear that working with two-level systems is the optimal way to develop computing power. The dimension of Hilbert space accessed by a quantum processor is a limitation on the complexity of problems it can solve. For N quantum elements each with d eigenstates, the dimensionality is d^N. We can increase the Hilbert space dimension by increasing N, the most conventional approach, or also by increasing d. Most quantum elements used for computing have access to many discrete eigenstates which can be used for computing, and actively suppress excitations outside of a two-level subspace. Quantum systems are inherently discrete, and their unitary gates are inherently continuous, requiring significant calibration to perform accurately. Thus, some benefits of reducing computational elements to two levels familiar from digital boolean logic don't apply to qubits.

A single qutrit can be represented as

$$|\psi\rangle = \begin{pmatrix} a \\ be^{i\phi_1} \\ ce^{i\phi_2} \end{pmatrix} \tag{2.4}$$

which after normalization ($a^2 + b^2 + c^2 = 1$) leaves four free parameters: $b, c \in [0, 1]$, $a^2 + b^2 \leq 1$ and $\phi_1, \phi_2 \in [0, 2\pi)$. Though visualizations have been developed for qutrits, there are none as clear as the Bloch sphere, since the

[1]Digital logic very strictly defines ranges of electric potential which are acceptable to represent $|0\rangle$ and $|1\rangle$ at the input of a logic gate, and more restricted ranges for its output.

state would be best visualized in 4 dimensions. Nevertheless, a qutrit gate can be seen as a direct extension of the SU(2) qubit gate to SU(3). The group SU(3) is generated by exponentiating the eight Gell-Mann matrices,

$$\begin{aligned}
\hat{\lambda}_1 &= \begin{pmatrix} 0 & 1 & 0 \\ 1 & 0 & 0 \\ 0 & 0 & 0 \end{pmatrix}, \quad \hat{\lambda}_2 = \begin{pmatrix} 0 & -i & 0 \\ i & 0 & 0 \\ 0 & 0 & 0 \end{pmatrix}, \\
\hat{\lambda}_4 &= \begin{pmatrix} 0 & 0 & 1 \\ 0 & 0 & 0 \\ 1 & 0 & 0 \end{pmatrix}, \quad \hat{\lambda}_5 = \begin{pmatrix} 0 & 0 & -i \\ 0 & 0 & 0 \\ i & 0 & 0 \end{pmatrix}, \\
\hat{\lambda}_6 &= \begin{pmatrix} 0 & 0 & 0 \\ 0 & 0 & 1 \\ 0 & 1 & 0 \end{pmatrix}, \quad \hat{\lambda}_7 = \begin{pmatrix} 0 & 0 & 0 \\ 0 & 0 & -i \\ 0 & i & 0 \end{pmatrix}, \\
\hat{\lambda}_3 &= \begin{pmatrix} 1 & 0 & 0 \\ 0 & -1 & 0 \\ 0 & 0 & 0 \end{pmatrix}, \quad \hat{\lambda}_8 = \frac{1}{\sqrt{3}} \begin{pmatrix} 1 & 0 & 0 \\ 0 & 1 & 0 \\ 0 & 0 & -2 \end{pmatrix}.
\end{aligned} \tag{2.5}$$

2.2 Atomic Physics

Atoms have been an invaluable tool for the study of quantum physics for over 100 years. All atoms of a particular species are *exactly* the same, and (especially *hydrogen-like* atoms) are well-studied and understood. This makes atoms an excellent platform on which to build quantum technology.

This section covers the energetic structure of ^{87}Rb, the alkali atom used in our experiments, in section 2.2.1. Two effects that perturb the energy level structure are discussed – the Zeeman effect (sec. 2.2.2) and the Stark effect (sec. 2.2.3). The last two sections discuss methods for state manipulation (2.2.4), and the state of neutral atom quantum computing (2.2.6).

2.2.1 Structure of ^{87}Rb

The information in this section is informed by Daniel A. Steck's self-published resource on ^{87}Rb [70].

Rubidium-87 is an alkali metal. It has 50 neutrons, 37 protons, and 37 electrons, one of which is unpaired in the valence shell, so the electronic spin $S = \frac{1}{2}$. With all lower levels filled, the valence electron has principal quantum number $n = 5$ when it is not excited. This work deals exclusively with $n = 5$.

The nucleus also has spin, $I = \frac{3}{2}$, so in the ground state where the electron orbital angular momentum $L = 0$, we have for the total angular momentum

$$\mathbf{F} = \mathbf{I} + \mathbf{S} = \frac{3}{2} \pm \frac{1}{2}.$$

If the nuclear and electronic spins are aligned, we have $F = 2$, and when they are anti-aligned, we have $F = 1$. This interaction between the angular momentum of the nucleus and the electron gives rise to the hyperfine structure. The hyperfine F-levels are shown in Figure 2.2a with their $2F + 1$ magentic sub-levels. The two manifolds are split by $\Delta E_{\mathrm{HF}} = h \cdot 6.835\,\mathrm{GHz}$.

2.2.2 Zeeman Effect

In the presence of a magnetic field, a perturbing term is added to the atomic Hamiltonian [3],

$$\hat{H}_Z = -\boldsymbol{\mu} \cdot \mathbf{B}, \tag{2.6}$$

where $\boldsymbol{\mu}$ is the magnetic dipole moment of the atom and $\mathbf{B}$ is the magnetic flux density. We operate exclusively in the low-$\mathbf{B}$ regime where the hyperfine splitting dominates $\hat{H}_Z$. We can use perturbation theory to calculate the first- and second-order corrections to the energies by starting with the λ-parameterized Hamiltonian

$$\hat{H}_{\mathrm{total}} = \hat{H}_0 + \lambda \hat{H}_Z, \tag{2.7}$$

where for the atomic Hamiltonian $\hat{H}_0$ we define the eigenenergies $E_{|F=1\rangle} = 0$, $E_{|F=2\rangle} = \hbar\omega_{\mathrm{HF}}$. Following the usual approach [8] we expand the Hamiltonian and states as a power series,

$$|\psi\rangle = |\psi^0\rangle + \lambda|\psi^1\rangle + \lambda^2|\psi^2\rangle + \ldots, \tag{2.8}$$

$$\hat{W} = \hat{W}^{(0)} + \lambda\hat{W}^{(1)} + \lambda^2\hat{W}^{(2)} + \ldots, \tag{2.9}$$

where $\hat{W}^{(n)}$ are the n order eigenvalues for the Hamiltonian, and $|\psi^n\rangle$ are the n order corrections to the eigenstates. The eigenvalue equation can be written as

$$(\hat{H}_0 + \lambda\hat{H}_Z)(|\psi^0\rangle + \lambda|\psi^1\rangle + \ldots) = (\hat{W}^{(0)} + \lambda\hat{W}^{(1)} + \ldots)(|\psi^0\rangle + \lambda|\psi^1\rangle + \ldots). \tag{2.10}$$

Gathering terms for λ, the zero-order term

$$\hat{H}_0|\psi^0\rangle = \hat{W}^0|\psi^0\rangle \tag{2.11}$$

is the unperturbed Schrödinger equation where $\hat{W}^0$ are the energies and $|\psi^0\rangle = |F, m_F\rangle$. To first order in λ, we can isolate the energy perturbation $\hat{W}^{(1)}$ which we call the "linear Zeeman shift"

$$\begin{aligned} \hat{H}_0|\psi^1\rangle + \hat{H}_Z|\psi^0\rangle &= \hat{W}^{(0)}|\psi^1\rangle + \hat{W}^{(1)}|\psi^0\rangle \\ \langle\psi^0|\hat{H}_Z|\psi^0\rangle &= \hat{W}^{(1)} \end{aligned} \tag{2.12}$$

because while $\hat{H}_0$ has several degenerate eigenvalues for each hyperfine level, it shares an eigenbasis with $\hat{H}_Z$ which are $|\psi^0\rangle = |F, m_F\rangle$. To second order, we have the "quadratic Zeeman shift" $\hat{W}^{(2)}$

$$\begin{aligned} \hat{H}_0|\psi^2\rangle + \hat{H}_Z|\psi^1\rangle &= \hat{W}^{(0)}|\psi^2\rangle + \hat{W}^{(1)}|\psi^1\rangle + \hat{W}^{(2)}|\psi^0\rangle \\ \hat{W}^{(0)}\langle\psi^0|\psi^1\rangle &= \hat{W}^{(1)}\langle\psi^0|\psi^1\rangle + \hat{W}^{(2)} \end{aligned} \tag{2.13}$$

which can be simplified by calculating $|\psi^1\rangle$, the first-order correction to the eigenstate.

To second order, we can write the Zeeman term in the Hamiltonian as [31]

$$\hat{H}_Z = \mu_B g_F m_F B_0 + \frac{(\mu_B g_F m_F B_0)^2}{\hbar\omega_{\mathrm{HF}}} \tag{2.14}$$

where μ_B is the Bohr magneton, g_F is the Landé g-factor for the hyperfine manifold F, and m_F is the magnetic quantum number defined along $\hat{z}$. The energetic level structure of the ground state of ^{87}Rb in the presence of a weak magnetic field is shown in figure 2.2b. In this work, the second-order Zeeman term is negligible, and we find adjacent m_F states split by roughly $h \cdot 1.25\,\mathrm{MHz}$ by a magnetic field of $\approx 1.8\,\mathrm{G}$.

2.2.3 Stark Effect

In the presence of an electric field, a perturbing term is added to the atomic Hamiltonian [3],

$$H_{\mathcal{E}} = -\mathbf{d} \cdot \mathcal{E}, \tag{2.15}$$

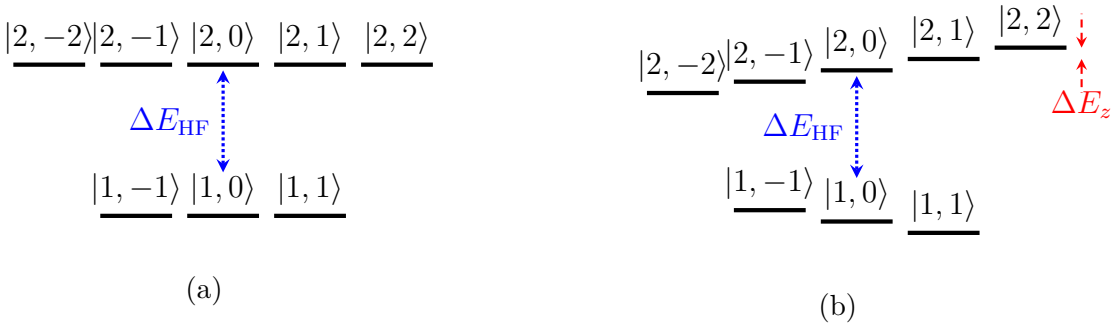

Figure 2.2: The structure of the ground state of ^{87}Rb with the $|F, m_F\rangle$ states labelled. (a) without an external magnetic field the m_F levels are degenerate, (b) with a weak magnetic field the degeneracy is lifted. ΔE_z is the linear Zeeman shift, $\hat{W}^{(1)}$. In this work, $\Delta E_{\mathrm{HF}} \approx 10^3 \Delta E_z$.

where $\mathbf{d}$ is the electric dipole operator and $\mathcal{E}$ is the electric field. Atoms are *polarizable*, i.e., an external electric field $\mathcal{E}$ will perturb the energy levels in the Hamiltonian analagously to magnetic fields perturbing energy levels via the Zeeman effect. Stark shifts take the form [3, 70]

$$E_{\mathrm{S}} = -\frac{1}{2}\alpha_0 \mathcal{E}^2 - \frac{1}{2}\alpha_2^F \mathcal{E}^2 \left[\frac{3m_F^2 - F(F+1)}{F(2F-1)}\right], \tag{2.16}$$

where α_0 is the static polarizability and α_2^F is the tensor polarizability of the hyperfine manifold F. Both of these are constants that can be found in [70].

2.2.4 State Manipulation Methods

The $|F, m_F\rangle$ state of ^{87}Rb within the ground state $5^2\mathrm{S}_{1/2}$ with weak-regime Zeeman splitting can be manipulated by radio-frequency magnetic fields of $\omega/2\pi \approx 10^6$ Hz, microwave-frequency magnetic fields of $\omega/2\pi \approx 10^{10}$ Hz, or optical electric fields of $\omega/2\pi \approx 10^{14}$ Hz.

Both the radio-frequency and microwave-frequency fields target magnetic dipole (M1) transitions. These transitions allow $\Delta m_F \in \{0, \pm 1\}$ and $\Delta F \in \{0, \pm 1\}$ within the ground-state manifold. When $\Delta F = 0$, we remain in the hyperfine manifold, and only the Zeeman splitting separates the states. As a result, the resonant coupling frequency ω_{RF} will directly relate to the difference in energy between the two coupled states contributed by the Zeeman term in the Hamiltonian eq. (2.14), $\Delta E_Z \approx \Delta m_F g_F \mu_B B_0$, $\omega_{\mathrm{RF}} = \Delta E_Z/\hbar$. At a weak

level of splitting the quadratic Zeeman term is negligible, and all adjacent m_F levels are equally coupled. When $\Delta F = \pm 1$, transitions are made across hyperfine levels, and the resonant frequency will be near the hyperfine splitting, $\Delta E_{\mathrm{HF}}/h = 6.835\,\mathrm{GHz}$. Even in the linear Zeeman regime, five of the nine transitions will have non-degenerate, unique resonant frequencies,

$$\omega_{|2,m_F\rangle|1,m'_F\rangle} = \omega_{\mathrm{HF}} + \frac{\mu_B B_0 (m_F + m'_F)}{2\hbar} \tag{2.17}$$

where we have considered only the hyperfine splitting and the linear Zeeman term, with two frequency degeneracies in the $\Delta F = \pm 1$ case we are considering,

$$\omega_{|2,0\rangle|1,1\rangle} = \omega_{|2,1\rangle|1,0\rangle},$$
$$\omega_{|2,0\rangle|1,-1\rangle} = \omega_{|2,-1\rangle|1,0\rangle}.$$

The $|F, m_F\rangle$ state can also be manipulated by a two-photon stimulated Raman transition. These transitions are conducted by two detuned electric dipole (E1) transitions through an intermediate upper level $|i\rangle$. With sufficient detuning, there are no excitations to $|i\rangle$, only the two-photon process occurs, which returns the atom to some new $|F', m'_F\rangle$ in the ground state. By selecting the frequencies, polarizations, and propagation direction of the two driving laser beams appropriately, these Raman transitions can achieve $\Delta F \in \{0, \pm 1\}$ and $\Delta m_F \in \{0, \pm 1, \pm 2\}$ if an appropriate intermediate upper level is available allowed by E1 selection rules.

2.2.5 Rabi Oscillations

Consider three levels within the ground state of ^{87}Rb, $|0\rangle = |F = 2, m_F = 2\rangle$ and $|1\rangle = |F = 1, m_F = 1\rangle$, and $|2\rangle = |F = 2, m_F = 1\rangle$ with linear Zeeman splitting. We can define a reference energy level based on state $|1\rangle$ such that the energy of $|1\rangle$ is 0. We can define the energy of state $|0\rangle$ $E_{\mathrm{A}} = \hbar\omega_{\mathrm{A}}$, and the energy of state $|2\rangle$ $E_{\mathrm{B}} = \hbar\omega_{\mathrm{B}}$. Radiation resonant with either of these transitions is non-resonant with any other transition in the atom. The magnetic field along $\mathbf{z}$ sets the Zeeman splitting. If we apply some perturbatory oscillating magnetic field *perpendicular* to $\mathbf{z}$ of frequency ω, an interaction term

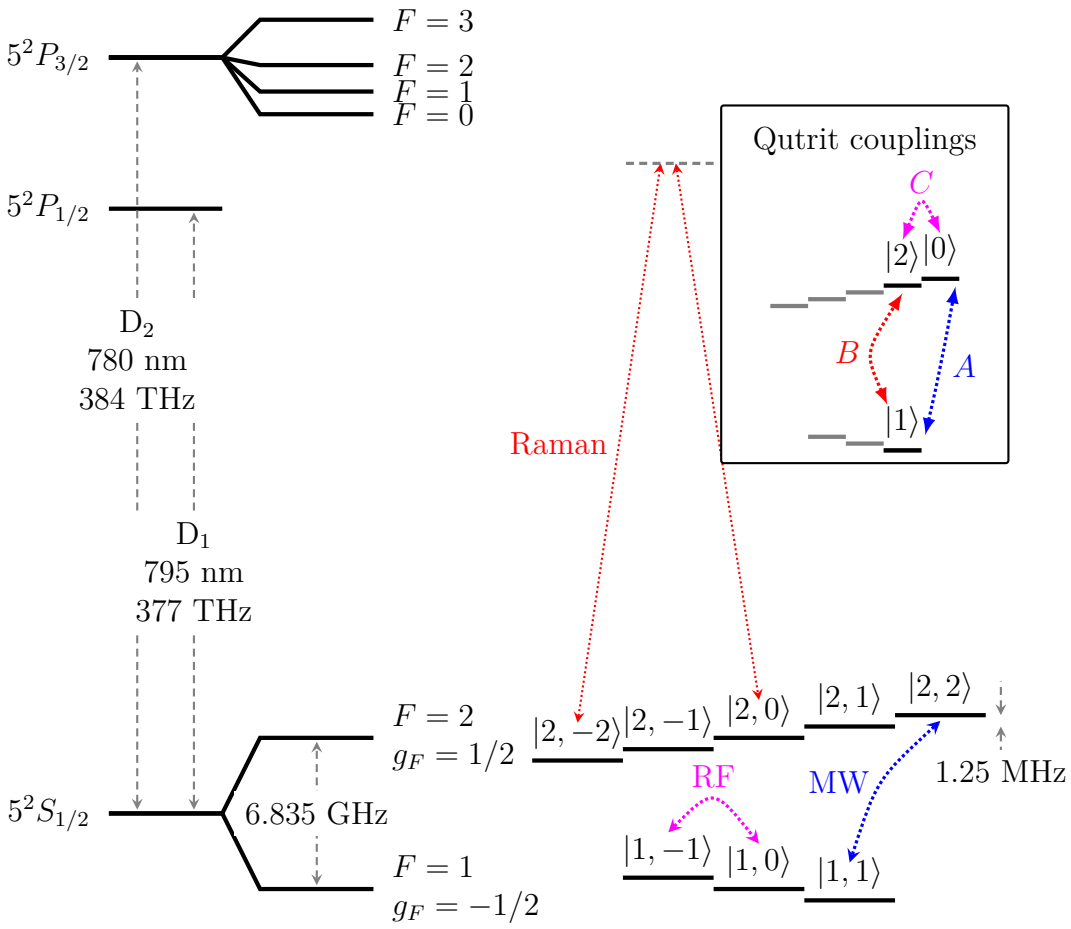

Figure 2.3: Level structure of ^{87}Rb with examples of possible state manipulations. Left: the two lowest orbital angular momentum levels S ($L = 0$), and P ($L = 1$). Fine structure, arising from the interaction of orbital and spin angular momentum $J = L + S$, splits the P levels into $J = 1/2$ and $J = 3/2$. Middle: hyperfine levels of the ground ($5^2S_{1/2}$) and D_2 excited states ($5^2P_{3/2}$). The hyperfine strucutre arises from the interaction of total electronic angular momentum J and nuclear angular momentum I. Right: Zeeman levels of the ground state which are split from degeneracy in the presence of an external magnetic field. The states are labelled $|F, m_F\rangle$. Methods of atomic state manipulation are superimposed. Radiofrequency (RF) magentic dipole transition with $\Delta F = 0$ in the linear Zeeman regime where all transitions are simultaneously resonant couple adjacent m_F states within one hyperfine manifold. Microwave (MW) magnetic dipole transition with $\Delta F = \pm 1$ couples states with $\Delta m_F = 0, \pm 1$. In red is a two-photon stimulated Raman transition. Two electric dipole transitions are driven at large detuning from resonance to one or more intermediate excited states as allowed by selection rules. Inset: the three qutrit levels and their coupling labelling convention, A, B, and C.

is added to the Hamiltonian,

$$\hat{H}_I = -\boldsymbol{\mu} \cdot \mathbf{B_0} \sin(\omega t + \phi). \tag{2.18}$$

The magnetic moment is

$$\boldsymbol{\mu} = -g_F \mu_B \hat{\mathbf{F}}/\hbar, \tag{2.19}$$

and defining the axes such that $\mathbf{B_0} = B_0 \mathbf{x}$, we have

$$\begin{aligned} \hat{H}_I &= \frac{g_F \mu_B B_0 \sin(\omega t + \phi)}{\hbar} \hat{F}_x \\ &= \frac{\hbar}{2} \begin{pmatrix} 0 & |\Omega_A| \sin(\omega t + \phi) & |\Omega_C| \sin(\omega t + \phi) \\ |\Omega_A| \sin(\omega t + \phi) & 0 & |\Omega_B| \sin(\omega t + \phi) \\ |\Omega_C| \sin(\omega t + \phi) & |\Omega_B| \sin(\omega t + \phi) & 0 \end{pmatrix} \end{aligned} \tag{2.20}$$

Since we are considering three transitions ($|0\rangle \leftrightarrow |1\rangle$,$|1\rangle \leftrightarrow |2\rangle$,$|0\rangle \leftrightarrow |2\rangle$), we have summed each of the above σ_x-type couplings in eq. (2.20). We have also defined the Rabi frequency's magnitude $|\Omega_X|$ from the matrix element $\hbar|\Omega_X| = -2\langle m|\boldsymbol{\mu} \cdot \mathbf{B_0}|n\rangle$ for each m, n, X.

The atomic Hamiltonian which describes the atomic structure (sec. 2.2.1) and includes the hyperfine interaction and Zeeman splitting (sec. 2.2.2) can be reduced to a diagonalized to $\hat{H}_{\text{at.}} = \hbar \, \text{diag}(\omega_A, 0, \omega_B)$. The full Hamiltonian is then

$$\begin{aligned} \hat{H} &= \hat{H}_{\text{at.}} + \hat{H}_I \\ &= \frac{\hbar}{2} \begin{pmatrix} \omega_A & |\Omega_A| \sin(\omega t + \phi) & |\Omega_C| \sin(\omega t + \phi) \\ |\Omega_A| \sin(\omega t + \phi) & 0 & |\Omega_B| \sin(\omega t + \phi) \\ |\Omega_C| \sin(\omega t + \phi) & |\Omega_B| \sin(\omega t + \phi) & \omega_B \end{pmatrix}. \end{aligned} \tag{2.21}$$

This Hamiltonian can be simplified by going into the *rotating frame* defined by

$$\hat{W} = \exp(it\hat{H}_{\text{at.}}/\hbar). \tag{2.22}$$

The transformation into this rotating frame, $\hat{\tilde{H}} = \hat{W}^\dagger \hat{H} \hat{W} + i\hbar(\partial_t \hat{W})\hat{W}^\dagger$, brings the Hamitonian to

$$\hat{\tilde{H}} = \frac{\hbar}{2} \begin{pmatrix} 0 & |\Omega_A| \sin(\omega t + \phi) e^{-i\omega_A t} & |\Omega_C| \sin(\omega t + \phi) e^{-i\omega_C t} \\ |\Omega_A| \sin(\omega t + \phi) e^{i\omega_A t} & 0 & |\Omega_B| \sin(\omega t + \phi) e^{i\omega_B t} \\ |\Omega_C| \sin(\omega t + \phi) e^{i\omega_C t} & |\Omega_B| \sin(\omega t + \phi) e^{-i\omega_B t} & 0 \end{pmatrix} \tag{2.23}$$

where we have defined $\omega_C = \omega_A - \omega_B$, and $\omega_C = \omega_{\mathrm{RF}}$ is the resonant frequency which couples states $|0\rangle$ and $|2\rangle$. For each of the three couplings in this Hamiltonian, we shall consider the case where $\omega \approx \omega_X$ (i.e. a near-resonant field) and the far-off resonance case. Let the detuning for each transition be $\Delta_X = \omega_X - \omega$.

Box 2.1: On the Phase of a Coupling Term

The Hamiltonian eq. (2.23) contains only coupling terms. It is important to understand what the meaning of the magnitude and phase of the coupling term will do when a qubit or qutrit is evolving. For simplicity, let us consider a slightly simpler two-level system,

$$\hat{\tilde{H}} = \frac{\hbar}{2}\begin{pmatrix} 0 & |\Omega|e^{i\varphi} \\ |\Omega|e^{-i\varphi} & 0 \end{pmatrix} = \frac{\hbar|\Omega|}{2}\left(\cos\varphi\hat{\sigma}_x + \sin\varphi\hat{\sigma}_y\right). \tag{2.24}$$

This expansion into the Pauli matrices $\hat{\sigma}_x$ and $\hat{\sigma}_y$ allows us to use the well-known formula for their exponentiation (the formula can be derived by series-expanding the functions),

$$e^{i\phi(\hat{n}\cdot\vec{\sigma})} = \hat{\mathbb{1}}\cos(\phi) + i(\hat{n}\cdot\vec{\sigma})\sin(\phi). \tag{2.25}$$

Thus we find the unitary evolution operator,

$$\begin{aligned} \hat{U} &= e^{it\hat{\tilde{H}}/\hbar} \\ &= \hat{\mathbb{1}}\cos\left(\tfrac{|\Omega|t}{2}\right) + i\sin\left(\tfrac{|\Omega|t}{2}\right)\left(\cos\varphi\hat{\sigma}_x + \sin\varphi\hat{\sigma}_y\right) \\ &= \begin{pmatrix} \cos\left(\tfrac{|\Omega|t}{2}\right) & i\sin\left(\tfrac{|\Omega|t}{2}\right)e^{i\varphi} \\ i\sin\left(\tfrac{|\Omega|t}{2}\right)e^{-i\varphi} & \cos\left(\tfrac{|\Omega|t}{2}\right) \end{pmatrix}. \end{aligned} \tag{2.26}$$

This operator rotates between the states $|0\rangle$ and $|1\rangle$. It can be visualized as a rotation on the Bloch sphere where the rotation axis is on the x-y plane, recall figure 2.1. The rotation frequency is $\frac{|\Omega|}{2}$, and the orientation of the rotation axis on the x-y plane is set by the phase of the coupling term, φ.

Now we can extend this understanding to the case where we have an oscillating $\varphi = \varphi(t) = a_\varphi\sin(\omega_\varphi t + \phi_\varphi)$. When the axis of rotation rotates much more quickly than rotation along the axis, the net effect is a precession of the state. In the limit $\omega_\varphi \gg |\Omega|$, the state will not evolve, and the Hamiltonian can be ignored.

Now consider the coupling terms $|\Omega_X|\sin(\omega t + \phi)e^{\pm i\omega_X t}$. We can visualize the effect of a coupling as drving a rotation on its SU(2) subspace by simply

setting all $|\Omega_Y|$ terms to zero. Their amplitude is $|\Omega_X|$, and the terms will oscillate in the complex plane following $\sin(\omega t + \phi)e^{\pm i\omega_X t}$. It can be helpful to expand out the sin to reveal two oscillating terms,

$$\hat{\tilde{H}}_{nm} = \frac{|\Omega_X|}{2}\left\{ie^{-i[(\omega\mp\omega_X)t+\phi]} - ie^{i[(\omega\pm\omega_X)t+\phi]}\right\}. \tag{2.27}$$

Now consider that in both the upper and lower sign versions of $\hat{\tilde{H}}_{nm}$, one term will have $\omega - \omega_X$, which is $-\Delta_X$, and the other term will have $\omega + \omega_X$, which is $2\omega - \Delta_X$.

$$\hat{\tilde{H}}_{nm} = \frac{i|\Omega_X|}{2}\begin{cases} e^{-i(-\Delta_X t+\phi)} - e^{i(2\omega t-\Delta_X t+\phi)}, & +\text{branch} \\ e^{-i(2\omega t-\Delta_X t+\phi)} - e^{i(-\Delta_X t+\phi)}, & -\text{branch} \end{cases}. \tag{2.28}$$

We will make the assumption that $2\omega - \Delta_X \gg |\Omega_X|$. This assumption is the *rotating wave approximation*. As we have seen in Box 2.1, terms which oscillate much more quickly than their Rabi frequencies can be eliminated from the Hamiltonian. The coupling is finally reduced to

$$\hat{\tilde{H}}_{nm} = \frac{i|\Omega_X|e^{\pm i\Delta_X t}e^{\mp i\phi}}{2}. \tag{2.29}$$

We can wrap in the $e^{i\phi}$ as the complex part of the Rabi frequency, $\Omega_X = |\Omega_X|e^{i\phi}$. The resonances for A, B, and C are all well separated from each other. The minimum spacing is between resonances is $\omega_A - \omega_B \approx 10^3|\Omega|$, which satisfies the far-detuned criteria. Thus any field resonant with another transition is always far-detuned. As a result, if $\omega \approx \omega_A$, the Hamiltonian eq. (2.23) reduces to

$$\tilde{H}_A = \frac{i\hbar}{2}\begin{pmatrix} 0 & -\Omega_A e^{-i\Delta_A t} & 0 \\ \Omega_A^* e^{i\Delta_A t} & 0 & 0 \\ 0 & 0 & 0 \end{pmatrix}. \tag{2.30}$$

Similar Hamiltonians would be found for transitions B and C.

With zero detuning, eq. (2.23) is a time-independent Hamiltonian, so the Schrödinger equation can be directly solved. Using transition A as an example,

$$\hat{U}_A(\chi,\phi) = \begin{pmatrix} \cos\left(\frac{\chi}{2}\right) & e^{i\phi}\sin\left(\frac{\chi}{2}\right) & 0 \\ e^{-i\phi}\sin\left(\frac{\chi}{2}\right) & \cos\left(\frac{\chi}{2}\right) & 0 \\ 0 & 0 & 1 \end{pmatrix} \tag{2.31}$$

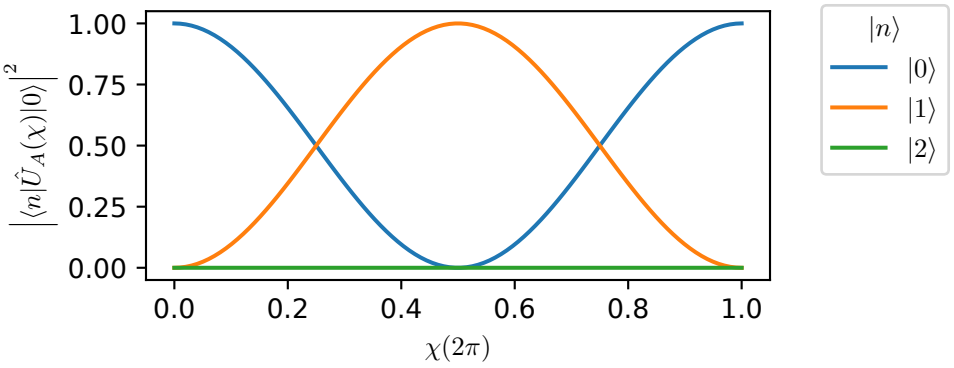

Figure 2.4: Rabi oscillations assuming an initial state $|0\rangle$ and $\omega = \omega_A$.

is the unitary evolution matrix where we have defined the *pulse area* $\chi = |\Omega_X|t$. The population evolution over a Rabi cycle is shown in figure 2.4 for resonance with ω_A and initial state $|0\rangle$.

In order to solve the dynamics of a system with detuning, it is convenient to perform a second change of basis from the $\hat{W}$ frame eq. (2.22) to the frame

$$\hat{Y} = \exp\left(\frac{it}{\hbar}(\hat{H}_{\text{at.}} - \hat{H}_\Delta)\right) \tag{2.32}$$

where

$$\hat{H}_\Delta = \hbar\,\text{diag}(\Delta_A, 0, \Delta_B). \tag{2.33}$$

We arrive at the rotating-frame Hamiltonian in $\hat{Y}$

$$\tilde{H}_Y = \frac{i\hbar}{2}\begin{pmatrix} -2i\Delta_A & -\Omega_A & -\Omega_C e^{it(\Delta_A-\Delta_B-\Delta_C)} \\ \Omega_A^* & 0 & \Omega_B^* \\ \Omega_C^* e^{-it(\Delta_A-\Delta_B-\Delta_C)} & -\Omega_B & -2i\Delta_B \end{pmatrix}. \tag{2.34}$$

If we set $\Omega_B = \Omega_C = 0$, then the Rabi oscillations starting in state $|0\rangle$ are demonstrated by figure 2.5. The figure shows that for oscillations with moderately high detuning ($|\Delta_X| > |\Omega_X|$) oscillation amplitude is significantly decreased compared to resonance, and suggests the conclusion we reached earlier that very high detunings will not couple the states.

2.2.6 Neutral Atom Quantum Computing

Currently, many technologies are being co-developed as platforms for quantum computing. These include superconducting processors (including those

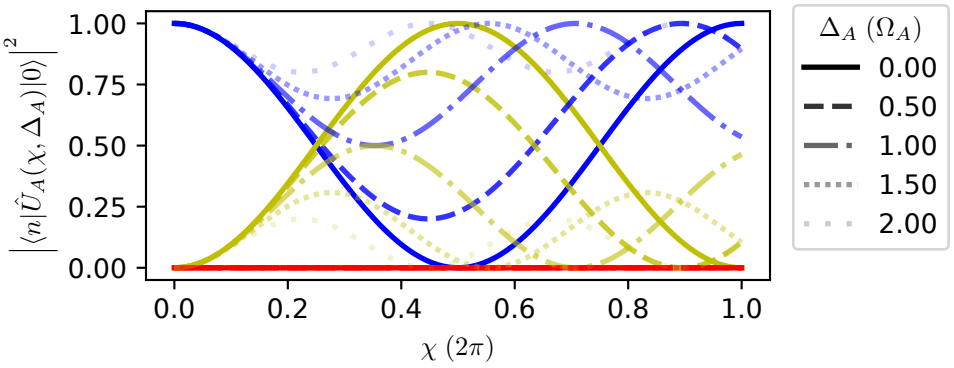

Figure 2.5: Rabi oscillations assuming an initial state $|0\rangle$ and $\omega = \omega_A - \Delta_A$.

produced by Anyon Systems, where I currently work), trapped ions (e.g. IonQ [22] and Quantinuum [62]), photonic systems (e.g. Xanadu [50] and Psi-Quantum [7]), and neutral atoms (e.g. QuEra [79]). While systems based on neutral atoms are generally less common and less developed, they boast significant potential for scalability.

While there are many superconducting qubit architectures being developed, current processors have at least one separate coaxial cable for every qubit. Since these processors operate in a dilution refrigerator where cable routing is a complex and expensive feat, connecting signals to each qubit will prove a challenge when scaling to higher qubit numbers. Manufacturing variability will also cause each qubit to have slightly different properties, making chip characterization and calibration a complicated endeavour.

Trapped ions systems boast good connectivity between qubits and very high gate fidelities, but the number of ions held in a trap is very constrained. To build large arrays of trapped ions, many traps are likely to be needed, which remains an open problem for trapped ion systems [15].

Neutral atom arrays benefit from having perfectly identical qubits. They can be trapped at the focus of a laser beam. Producing an arbitrary number of traps is trivial, and groups have developed highly parallelized gates for control [11].

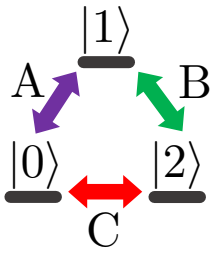

Figure 2.6: Labelling convention for the three couplings on a qutrit.

2.3 Arbitrary Qutrit Gates

A single qutrit gate (sec. 2.1.3) is significantly more complicated to produce than a single qubit gate (sec. 2.1.2), i.e. it is the result of 8 generators rather than 3. We will show how a desired unitary $\hat{U}_{\text{target}}$ can be produced by decomposing the operation into SU(2) steps in section 2.3.1 and how "virtual" phase gates can be generated to apply some phase to each eigenstate (sec. 2.3.2). We will derive the dual-tone operator (2.3.3).

2.3.1 SU(2) Decompositions

One method of producing any arbitrary qutrit unitary is to decompose it into 3 consecutive unitaries on two-level subspaces followed by a phase gate [25, 41, 42, 54, 74, 81]. The three two-level couplings in a qutrit are labelled A, B, and C according to figure 2.6. There are many ways to combine unitaries on each of these subspaces for full control, for example,

$$\hat{U}^{\text{I}} = \hat{U}_\theta(\eta,\varepsilon)\hat{U}_{\text{B}}(\chi_{\text{B2}},\varphi_{\text{B2}})\hat{U}_{\text{A}}(\chi_{\text{A1}},\varphi_{\text{A1}})\hat{U}_{\text{B}}(\chi_{\text{B1}},\varphi_{\text{B1}}) \tag{2.35}$$

where $\hat{U}_{\text{X}}$ denotes a SU(2) unitary on coupling X, χ and φ are the pulse area and phase of the gate, and $\hat{U}_\theta$ is a diagonal phase gate,

$$\hat{U}_\theta(\eta,\varepsilon) = \begin{pmatrix} e^{i\eta} & 0 & 0 \\ 0 & e^{i\varepsilon} & 0 \\ 0 & 0 & e^{-i(\eta+\varepsilon)} \end{pmatrix}. \tag{2.36}$$

Another equally valid decomposition is

$$\hat{U}^{\text{II}} = \hat{U}_\theta(\eta,\varepsilon)\hat{U}_{\text{B}}(\chi_{\text{B}},\varphi_{\text{B}})\hat{U}_{\text{A}}(\chi_{\text{A}},\varphi_{\text{A}})\hat{U}_{\text{C}}(\chi_{\text{C}},\varphi_{\text{C}}). \tag{2.37}$$

Table 2.1: Parameters for Operator Decomposition

Decomposition	Step, k	$\hat{U}_k$	a	Coupling basis $\{\|\, m \,\rangle, \|\, n \,\rangle\}$
$\hat{U}^{\mathrm{I}} = \hat{U}_\theta \hat{U}_B \hat{U}_A \hat{U}_B$	1	$\hat{U}_{\text{target}}$	$\|0\rangle$	B: $\{\|1\rangle, \|2\rangle\}$
	2	$\hat{U}_{\text{target}} \hat{U}_1^\dagger$	$\|0\rangle$	A: $\{\|0\rangle, \|1\rangle\}$
	3	$\hat{U}_{\text{target}} \hat{U}_1^\dagger \hat{U}_2^\dagger$	$\|1\rangle$	B: $\{\|1\rangle, \|2\rangle\}$
$\hat{U}^{\mathrm{II}} = \hat{U}_\theta \hat{U}_A \hat{U}_B \hat{U}_C$	1	$\hat{U}_{\text{target}}$	$\|2\rangle$	C: $\{\|0\rangle, \|2\rangle\}$
	2	$\hat{U}_{\text{target}} \hat{U}_1^\dagger$	$\|2\rangle$	B: $\{\|1\rangle, \|2\rangle\}$
	3	$\hat{U}_{\text{target}} \hat{U}_1^\dagger \hat{U}_2^\dagger$	$\|1\rangle$	A: $\{\|0\rangle, \|1\rangle\}$

The method for decomposing these SU(2) couplings was provided in the supplementary material of [42] with typographical errors, which have been corrected here.

The general method behind the algorithm is as follows. For a target unitary $\hat{U}_{\text{target}}$ and some decomposition $\hat{U}_{\text{decomp.}} = \hat{U}_\theta \hat{U}_3 \hat{U}_2 \hat{U}_1$, we apply the terms of $\hat{U}_{\text{decomp.}}^\dagger$ such that $\hat{U}_{\text{target}} \hat{U}_1^\dagger$ has at least one off-diagonal zero, $\hat{U}_{\text{target}} \hat{U}_1^\dagger \hat{U}_2^\dagger$ has at least four, $\hat{U}_{\text{target}} \hat{U}_1^\dagger \hat{U}_2^\dagger \hat{U}_3^\dagger$ has none, and $\hat{U}_{\text{target}} \hat{U}_{\text{decomp.}}^\dagger = \mathbb{1}$.

An SU(2) coupling on the basis $\{\|\, m \,\rangle, \|\, n \,\rangle\}$ of area χ and phase ϕ can be expressed as

$$\hat{U}^{mn}(\chi, \phi) = \exp\left\{-i\frac{\chi}{2}\left[\cos(\phi)\hat{\sigma}_x^{mn} + \sin(\phi)\hat{\sigma}_y^{mn}\right]\right\} \tag{2.38}$$

where $\hat{\sigma}_x^{mn} = |m\rangle\langle n| + |n\rangle\langle m|$ and $\hat{\sigma}_y^{mn} = i|n\rangle\langle m| - i|m\rangle\langle n|$. Each step of the decomposition has the rotation angle set to

$$\chi = 2 \arcsin \sqrt{\frac{|\langle a|\hat{U}_k|m\rangle|^2}{|\langle a|\hat{U}_k|m\rangle|^2 + |\langle a|\hat{U}_k|n\rangle|^2}} \tag{2.39}$$

and the phase set to

$$\phi = \frac{\pi}{2} + \arg\left(\langle a|\hat{U}_k|m\rangle\right) - \arg\left(\langle a|\hat{U}_k|n\rangle\right) \tag{2.40}$$

where $\langle a|\hat{U}_k|m\rangle$ is a matrix element of $\hat{U}_k$ to be zeroed and $\hat{U}_k$ is the remaining remaining portion of $\hat{U}_{\text{target}}$ to be implemented. The values of $|a\rangle$, $|m\rangle$, $|n\rangle$, and $\hat{U}_k$ to be used for each step of the decomposition are given in Table 4.4.

2.3.2 Virtual Phase Gates

While [41] suggests applying far-off resonance fields to perform the phase gate (see eq. (2.36)), modern qutrit experiments [42, 81] implement diagonal phase gates virtually, rather than by directly manipulating the atoms. These virtual phase gates have zero duration and zero error.

Any unitary operators $\hat{U}_{\text{after}}$ that are to be implemented after phase gate $\hat{U}_\theta$ are simply phase shifted by the transform

$$\tilde{U}_{\text{after}} = \hat{U}_\theta^\dagger \hat{U}_{\text{after}} \hat{U}_\theta. \tag{2.41}$$

This effectively "delays" application of the $\hat{U}_\theta$ operator until the end of the pulse sequence by modifying each unitary.

$$\begin{aligned} &= \hat{U}_1 \hat{U}_2 \hat{U}_3 \hat{U}_\theta \hat{U}_5 \\ &= \hat{U}_\theta \hat{U}_\theta^\dagger \hat{U}_1 \hat{U}_\theta \hat{U}_\theta^\dagger \hat{U}_2 \hat{U}_\theta \hat{U}_\theta^\dagger \hat{U}_3 \hat{U}_\theta \hat{U}_5 \\ &= \hat{U}_\theta \tilde{U}_1 \tilde{U}_2 \tilde{U}_3 \hat{U}_5 \end{aligned} \tag{2.42}$$

The final $\hat{U}_\theta$ operator never needs to be applied because after the last operator, the state is projected via $\left\langle \psi \left| U_{\text{all}}^\dagger \right| n \right\rangle \langle n | U_{\text{all}} | \psi \rangle$, and the phase information is destroyed.

Several virtual phase gates are easily combined because $\hat{U}_{\theta,\text{net.}} = \hat{U}_{\theta,2} \hat{U}_{\theta,1}$ is also a valid virtual phase gate.

One may be interested to know whether we have found a mathematical curiosity or a useful tool for avoiding direct application of phase gates. Let us consider the effect of the transformation eq. (2.41) on each step of the SU(2)

decomposition. If we have some coupling on A with phase ϕ and pulse area χ,

$$\begin{aligned}
&\tilde{U}_A(\chi,\phi) = \hat{U}_\theta^\dagger \hat{U}_A(\chi,\phi)\hat{U}_\theta \\
&= \begin{pmatrix} e^{-i\eta} & 0 & 0 \\ 0 & e^{-i\varepsilon} & 0 \\ 0 & 0 & e^{i(\eta+\varepsilon)} \end{pmatrix} \begin{pmatrix} \cos(\frac{\chi}{2}) & -e^{i\phi}\sin(\frac{\chi}{2}) & 0 \\ e^{-i\phi}\sin(\frac{\chi}{2}) & \cos(\frac{\chi}{2}) & 0 \\ 0 & 0 & 1 \end{pmatrix} \begin{pmatrix} e^{i\eta} & 0 & 0 \\ 0 & e^{i\varepsilon} & 0 \\ 0 & 0 & e^{-i(\eta+\varepsilon)} \end{pmatrix} \\
&= \begin{pmatrix} \cos(\frac{\chi}{2}) & -e^{i(\phi+\varepsilon-\eta)}\sin(\frac{\chi}{2}) & 0 \\ e^{-i(\phi+\varepsilon-\eta)}\sin(\frac{\chi}{2}) & \cos(\frac{\chi}{2}) & 0 \\ 0 & 0 & 1 \end{pmatrix} \\
&= \hat{U}_A(\chi, \phi+\varepsilon-\eta).
\end{aligned} \tag{2.43}$$

So we have shown that the only effect is a change of phase on this transition, $\tilde{\phi}_A = \phi_A + \varepsilon - \eta$. In other words, we can implement the virtual phase gate by phase shifting the pulse. This property extends to B and C transitions with $\tilde{\phi}_B = \phi_B + \eta + 2\varepsilon$ and $\tilde{\phi}_C = \phi_C - \varepsilon - 2\eta$.

2.3.3 Dual-Tone Operator

Instead of the single-toned applied field of eq. (2.18), consider an applied magnetic field with two tones,

$$\mathbf{B} = \mathbf{B_A}\sin\left[(\omega_A - \Delta_A)t + \phi_A\right] + \mathbf{B_B}\sin\left[(\omega_B - \Delta_B)t + \phi_B\right]. \tag{2.44}$$

We can treat the two terms separately as we did in eq. (2.30) to form the simplified rotating wave Hamiltonian

$$\tilde{H} = \frac{i\hbar}{2}\begin{pmatrix} 0 & -\Omega_A e^{-i\Delta_A t} & 0 \\ \Omega_A^* e^{\Delta_A t} & 0 & \Omega_B^* e^{i\Delta_B t} \\ 0 & -\Omega_B e^{-i\Delta_A t} & 0 \end{pmatrix}. \tag{2.45}$$

The operation caused by applying this Hamiltonian at dual-resonance ($\Delta_A = \Delta_B = 0$) is:

$$\hat{U}_{AB} = \exp(-i\tilde{H}t/\hbar) \tag{2.46}$$

$$= \begin{pmatrix} \cos(\frac{\chi_{\mathrm{AB}}}{2}) & 0 & -e^{i\varphi_{\mathrm{AB}}}\sin(\frac{\chi_{\mathrm{AB}}}{2}) \\ 0 & -1 & 0 \\ -e^{-i\varphi_{\mathrm{AB}}}\sin(\frac{\chi_{\mathrm{AB}}}{2}) & 0 & -\cos(\frac{\chi_{\mathrm{AB}}}{2}) \end{pmatrix} \tag{2.47}$$

where we have set the duration of the pulse $t_{AB} = \frac{2\pi}{\sqrt{|\Omega_1|^2+|\Omega_2|^2}}$ and defined

$$\chi_{\mathrm{AB}} = \arctan\left|\frac{\Omega_A}{\Omega_B}\right|, \tag{2.48}$$

$$\varphi_{\mathrm{AB}} = \arg\left(\frac{\Omega_A}{\Omega_B}\right). \tag{2.49}$$

The operation $\hat{U}_{AB}$ was discussed in [41] in the context of ion trap quantum computing. The evolution operator has the form of an effective coupling on C,

$$\hat{U}_C = \begin{pmatrix} \cos\left(\frac{\chi}{2}\right) & 0 & e^{i\phi}\sin\left(\frac{\chi}{2}\right) \\ 0 & 1 & 0 \\ e^{-i\phi}\sin\left(\frac{\chi}{2}\right) & 0 & \cos\left(\frac{\chi}{2}\right) \end{pmatrix}, \tag{2.50}$$

with an additional phase flip on the first element. We can thus synthesize an effective C coupling by applying fields at frequencies A and B only.

2.4 Tomography

Because readout of a quantum system is a projective process, information about a quantum state is destroyed during measurement, making characterization a non-trivial task. If we have many identical copies of the density matrix $\hat{\rho}$, this characterization can be done using quantum state tomography [57].

2.4.1 Density Matrices

A density matrix is a representation of a quantum system which is more general than a ket $|\psi\rangle$, capturing the *purity* ($\frac{1}{d} \leq \mathcal{P} \leq 1$) of the system. When $\mathcal{P} = 1$ we have a *pure state* which can be represented as a ket $|\psi\rangle$, and when $\mathcal{P} < 1$ we have a *mixed state* which must be represented by a density matrix. The density matrix of a pure state can be derived from its ket,

$$\hat{\rho} = |\psi\rangle\langle\psi|, \tag{2.51}$$

and the purity of a density matrix can be calculated simply,

$$\mathcal{P} = \mathrm{Tr}(\hat{\rho}^2). \tag{2.52}$$

The trace of a density matrix is always 1, and in the Schrödinger picture its evolution is simply

$$\hat{\rho}_2 = \hat{U}\hat{\rho}_1\hat{U}^\dagger. \tag{2.53}$$

In order to take some projection $|\xi\rangle\langle\xi|$ on some density matrix $\hat{\rho}$, we take the trace of their product

$$\mathrm{Tr}\left(|\xi\rangle\langle\xi|\hat{\rho}\right). \tag{2.54}$$

It is trivial to show that this reduces to $|\langle\xi|\psi\rangle|^2$ in the case of a pure state.

Mixed states can be used to represent the collective behaviour of an ensemble of pure states [63]. In the case of a qubit, a mixed state can be drawn as a vector on the Bloch sphere where the direction is set by its projection to the nearest pure state, and the length is the purity.

In analogy to the Bloch sphere representation of a qubit, the density matrix of a qubit can be written as a linear combination of the Pauli matrices and the identity matrix [73],

$$\hat{\rho}_{\mathrm{qubit}} = \frac{1}{2} + \frac{1}{2}\sum_{k=1}^{3} r_k\hat{\sigma}_k \tag{2.55}$$

where $\hat{\sigma}_{1,2,3}$ are the Pauli matrices, and r_k are the projections of the state on the Pauli matrices. This can be extended to the Gell-Mann matrices for a qutrit [73],

$$\hat{\rho}_{\mathrm{qutrit}} = \frac{1}{3} + \frac{1}{3}\sum_{k=1}^{8} r_k\hat{\lambda}_k \tag{2.56}$$

where $\hat{\lambda}_k$ are the Gell-Mann matrices eq. (2.5), and $r_k = \mathrm{Tr}(\hat{\lambda}\hat{\rho})$.

2.4.2 Qutrit Projections

After some density matrix $\hat{\rho}$ is prepared by some experiment, it can be measured directly by projection eq. (2.54) onto the computational basis states $|0\rangle$, $|1\rangle$, $|2\rangle$. Doing this directly can determine the final state populations, but will not reveal the phase relationship between the states or the purity. In order to fully characterize the density matrix, measurements must be made outside of the computational basis.

In order to read-out these phases, a simple $\chi = \pi/2$ area pulses can be performed between the states. One potential set of $\pi/2$-area pulses that can be used to characterize a qutrit is given in table 2.2.

Table 2.2: Read-out operators to characterize a qutrit state

$\hat{R}_k$	Basis	Phase ϕ	Matrix form
$\hat{R}_1$	$\{\|0\rangle, \|1\rangle\}$	0	$\frac{1}{\sqrt{2}}\begin{pmatrix} 1 & -1 & 0 \\ 1 & 1 & 0 \\ 0 & 0 & \sqrt{2} \end{pmatrix}$
$\hat{R}_2$	$\{\|0\rangle, \|1\rangle\}$	$\frac{\pi}{2}$	$\frac{1}{\sqrt{2}}\begin{pmatrix} 1 & -i & 0 \\ -i & 1 & 0 \\ 0 & 0 & \sqrt{2} \end{pmatrix}$
$\hat{R}_3$	$\{\|1\rangle, \|2\rangle\}$	0	$\frac{1}{\sqrt{2}}\begin{pmatrix} \sqrt{2} & 0 & 0 \\ 0 & 1 & 1 \\ 0 & -1 & 1 \end{pmatrix}$
$\hat{R}_4$	$\{\|1\rangle, \|2\rangle\}$	$\frac{\pi}{2}$	$\frac{1}{\sqrt{2}}\begin{pmatrix} \sqrt{2} & 0 & 0 \\ 0 & 1 & -i \\ 0 & -i & 1 \end{pmatrix}$
$\hat{R}_5$	$\{\|0\rangle, \|2\rangle\}$	0	$\frac{1}{\sqrt{2}}\begin{pmatrix} 1 & 0 & -1 \\ 0 & -\sqrt{2} & 0 \\ -1 & 0 & -1 \end{pmatrix}$
$\hat{R}_6$	$\{\|0\rangle, \|2\rangle\}$	$\frac{\pi}{2}$	$\frac{1}{\sqrt{2}}\begin{pmatrix} 1 & 0 & -i \\ 0 & -\sqrt{2} & 0 \\ i & 0 & -1 \end{pmatrix}$

In order to show that the operators of table 2.2 form a complete set, it is sufficient to show that the parameters r_k can be determined based on the projections of the read-out operators chosen. This is demonstrated in table 2.3.

Table 2.3: Demonstration of the Gell-Mann matrices constructed using read-out operators $\hat{R}_k$.

$\hat{\lambda}_k$	Construction
$\hat{\lambda}_1$	$\hat{R}_1^\dagger \left(\|1\rangle\langle 1\| - \|0\rangle\langle 0\|\right) \hat{R}_1$
$\hat{\lambda}_2$	$\hat{R}_2^\dagger \left(\|0\rangle\langle 0\| - \|1\rangle\langle 1\|\right) \hat{R}_2$
$\hat{\lambda}_3$	$\hat{R}_3^\dagger \|2\rangle\langle 2\| \hat{R}_3 - \hat{R}_5^\dagger \|1\rangle\langle 1\| \hat{R}_5{}^2$
$\hat{\lambda}_4$	$\hat{R}_5^\dagger \left(\|2\rangle\langle 2\| - \|0\rangle\langle 0\|\right) \hat{R}_5$
$\hat{\lambda}_5$	$\hat{R}_6^\dagger \left(\|0\rangle\langle 0\| - \|2\rangle\langle 2\|\right) \hat{R}_6$
$\hat{\lambda}_6$	$\hat{R}_3^\dagger \left(\|1\rangle\langle 1\| - \|2\rangle\langle 2\|\right) \hat{R}_3$
$\hat{\lambda}_7$	$\hat{R}_4^\dagger \left(\|1\rangle\langle 1\| - \|2\rangle\langle 2\|\right) \hat{R}_4$
$\hat{\lambda}_8$	$\left(\hat{R}_3^\dagger \|0\rangle\langle 0\| \hat{R}_3 + \hat{R}_5^\dagger \|1\rangle\langle 1\| \hat{R}_5 - 2\hat{R}_1^\dagger \|2\rangle\langle 2\| \hat{R}_1\right) / \sqrt{3}^3$

2.4.3 Maximum Likelihood Iteration

The tomographic measureents of table 2.2 are an over-complete set. Performing each read-out measurement will determine three parameters – the projection on each $|0\rangle$, $|1\rangle$, and $|2\rangle$. By measuring with six read-out operators, this tomographic measurement will set 18 parameters, while a fully-specified qutrit density matrix depends on only 8 real parameters. We determine the density matrix using a maximum likelihood method specified in [49].

This iterative method starts from the maximally mixed density matrix $\hat{\rho} = \frac{\mathbb{1}}{3}$ and updates using the equation

$$\hat{\rho}_{k+1} = \frac{\hat{Q}(\hat{\rho}_k)\hat{\rho}_k\hat{Q}(\hat{\rho}_k)}{\mathrm{Tr}\left(\hat{Q}(\hat{\rho}_k)\hat{\rho}_k\hat{Q}(\hat{\rho}_k)\right)} \tag{2.57}$$

where $\hat{Q}(\hat{\rho})$ is defined

$$\hat{Q}(\hat{\rho}) = \sum_k \sum_{n=0,1,2} \frac{f_n^k}{\mathrm{Tr}\left(\hat{R}_k^\dagger |n\rangle\langle n| \hat{R}_k \hat{\rho}\right)} \hat{R}_k^\dagger |n\rangle\langle n| \hat{R}_k. \tag{2.58}$$

Here, $\hat{R}_k$ is the read-out operator, and f_n^k is the experimentally-measured final population in state $|n\rangle$ after read-out operator k.

Chapter 3

Experimental Techniques

This chapter outlines the details of the qutrit experiment. It begins by discussing the most important parts of the *Quantum Simulation* apparatus used for this experiment, then discusses the calibration of operators.

3.1 Apparatus

The system used to generate cold atoms used for this experiment was thoroughly described by T. Hrushevskyi in his thesis [37]. More details on the design, construction and commissioning of the apparatus can be found there. This section outlines at a high level the techniques used to generate an atomic ensemble of atoms in their ground state, manipulate those atoms using microwaves, and read out their final state.

3.1.1 Preparation

Roughly every 30 s, the experimental apparatus prepares a new cloud of $\sim 10^5$ atoms in their ground state with $|F = 2, m_F = 2\rangle$.

The experiment is conducted inside an ultra-high vaccuum chamber, with pressure below 10^{-9} torr. Within the chamber is a sample of rubidium metal. When heated, some atoms vaporize in the chamber. A push-beam which is blue-detuned to the D_2 transition is resonant with atoms travelling away from the beam, and imparts some additional +x momentum on them. These atoms are directed towards the 2-D magneto-optical trap which reduces their

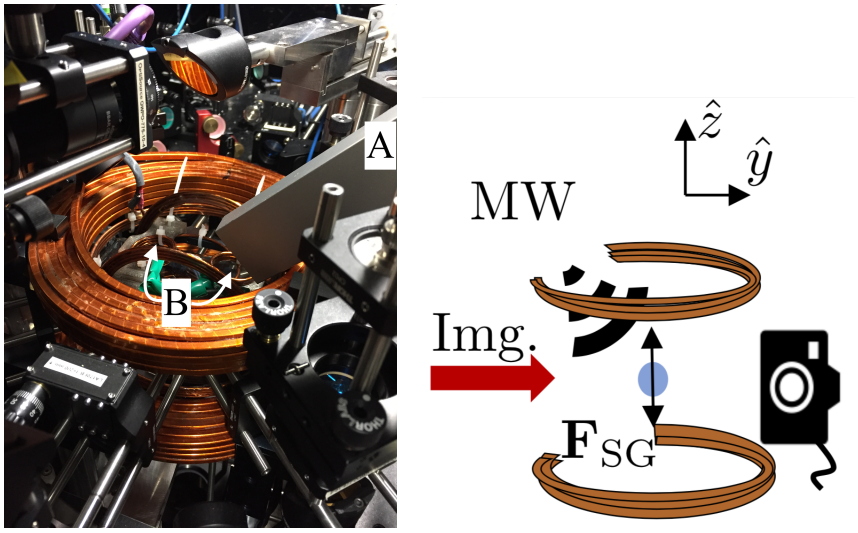

(a) (b)

Figure 3.1: (a) Experimental chamber (center) with supporting laser and magnetic infrastructure. The open-ended microwave waveguide is labelled A, and a set of RF-coils producing an x-directional field is labelled B. (b) Diagram of experimental chamber including the anti-Helmholtz coils, microwave (MW) waveguide input, imaging beam (Img.), CCD camera, atomic cloud (blue), and the direction of the Stern-Gerlach force $\mathbf{F}_{\mathrm{SG}}$.

momentum in the $\hat{z}$ and $\hat{y}$ directions. They then pass into a 3-D magneto-optical trap which holds them and cools them to around 50 µK. From there, several stages of evaporation are performed to selectively remove the most energetic atoms, leaving behind a cooled cloud. In the process, the atoms are transferred into a two-beam crossed optical dipole trap which holds them in an approximately Gaussian-shaped potential. These atoms are held within a Thomas-Fermi radius of approximately 6.5 µm.

An initial state of $|F = 2, m_F = 2\rangle$ is prepared by *optical pumping*. This makes use use of the *cycling transition* from the ground state $F = 2$ to $5^2P_{3/2}, F = 3$ (abbreviated to $F' = 3$) with polarization set for σ^+. Consider a scenario where an atom is at $|F = 2, m_F = -1\rangle$. When it absorbs a photon, it will be in the state $|F' = 3, m_F = 0\rangle$. It can de-excite to either $|F = 2, m_F = -1\rangle$ (where it started), or to $|F = 2, m_F = 0\rangle$, or $|F = 2, m_F = 1\rangle$. These rates will depend on the Clebsch-Gordan coefficients associated with those transitions, but the average effect will be an increase in m_F. After many

repetitions the atom will tend towards the state $|F = 2, m_F = 2\rangle$. At this point, absorbing a photon will bring it to $|F' = 3, m_F = 3\rangle$, which only has one electric-dipole-allowed de-excitation transition, back to $|F = 2, m_F = 2\rangle$. Thus the atom has entered a cycle, and can continue absorbing and re-emitting photons indefinitely. After many cycles, the atom has been *optically pumped* into the state $|F = 2, m_F = 2\rangle$. If the atom begins in $|F = 1\rangle$, a second *re-pump* laser which is resonant with the $|F = 1\rangle \rightarrow |F' = 2\rangle$ transition can be applied. The atoms could then probabilistically decay into either $|F = 2\rangle$ (where they would join the cycle), or back to $|F = 1\rangle$. With both lasers applied, regardless of which $|F, m_F\rangle$ state at the beginning of pumping, after many absorption and re-emission cycles the atom will be transferred to $|F = 2, m_F = 2\rangle$.

3.1.2 Microwave Generation

Microwaves are directed towards the atomic cloud using an open-ended waveguide, not aligned with any experimental axis, and resulting in an effectively unpolarized beam, as shown in figure 3.1a.

Microwave signals are produced using amplitude modulation between an arbitrary waveform generator and a microwave signal generator. The carrier frequency is generated by a Berkeley Nucleonics Model 845 Microwave Signal generator detuned to 100 MHz below the hyperfine splitting ω_{HF}. The baseband signal is an arbitrary waveform generated by Python software and uploaded to a Tektronix AWG5204 5 GS/s arbitrary waveform generator. The frequency offset of 100 MHz was chosen to ensure that all unwanted sidebands will be far-detuned from any atomic resonances.

An image of the microwave generation system is shown in figure 3.2. The *Quantum Simulation* apparatus is used simultaneously by a variety of projects. In the interest of ensuring that other experiments are able to operate reliably, the pre-existing microwave apparatus has not been significantly modified from its initial state. For this project, the only modification made to microwave system is the replacement of a simple RF digital direct synthesizer with the

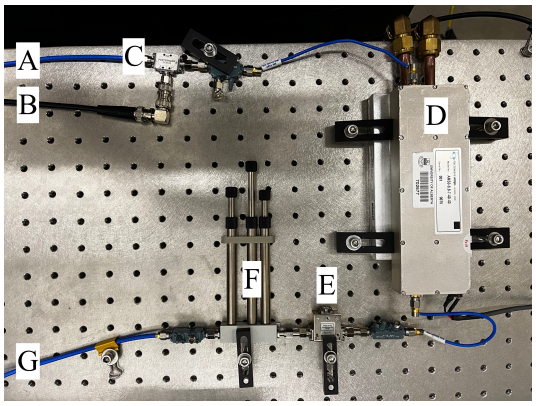

Figure 3.2: The microwave generation system. (A) input from the microwave signal generator. (B) input from the arbitrary waveform generator. (C) microwave mixer (D) amplifier (E) isolator (F) stub tuner (G) output to waveguide.

AWG5204, and integration of the AWG5204 into the system by writing a Python package. The main microwave amplifier is a water-cooled Microwave Amps Ltd. AM53-6.6-7-7-40. Its output power can be as high as 40 dBm, but this is shared across the entire signal, which will include both the upper (desired) sideband and the lower sideband. Additionally, when the AWG5204 is being used to generate a multi-tone signal, e.g. $f(t) = a_1 \sin(\omega_1 t + \phi_1) + a_2 \sin(\omega_2 t + \phi_2)$, the full signal spectrum received by the microwave amplifier includes sum and differences of $\omega_{\mathrm{HF}} - 2\pi 100\,\mathrm{MHz}$, $\omega_1 + 2\pi 100\,\mathrm{MHz}$, and $\omega_2 - 2\pi 100\,\mathrm{MHz}$ in all combinations (see figure 3.5 for spectrum analyzer readings). In order to not "waste" amplification on unused spectral components, we could insert a high-pass filter after the mixer with a cut-off frequency slightly above the carrier frequency. Future users of this device should also be aware of the potential limitations of the power amplifier's power supply. When applying a simple resonant Rabi pulse, it was observed that the duration of the first π period is shorter than that of the second π period, or the third π period. The Rabi frequency appears to decrease as a function of the amplifier's on-time which might suggest that the power supply or the amplifier is not well-suited to the intermittent yet high-power control pulses.

3.1.3 State Readout

The final state of the ensemble is read out using *Stern-Gerlach imaging* which consists of applying an m_F-dependent force to the ensemble to separate the states spatially, then probing with a resonant imaging beam and capturing the absorption image on a CCD camera.

After state preparation and manipulation, the imaging sequence begins by turning on the anti-Helmholtz coils which creates a magnetic field gradient ∇B along all axes ($\hat{z}$ and $\hat{r}$). This spatially-dependent field means there is a spatially-dependent potential associated with the Zeeman Hamiltonian, which is the force,

$$\begin{aligned} \mathbf{F}_{\mathrm{SG}} &= -\nabla U \\ &= -\nabla(-\boldsymbol{\mu} \cdot \mathbf{B_0}) \\ &= \frac{g_F m_F \mu_B}{\hbar} \partial_z B_0. \end{aligned} \tag{3.1}$$

Thus the $|F, m_F\rangle$ states experience a force proportional to the product $g_F m_F$. Once the anti-Helmholtz coils have been turned on, the atoms are then released from the optical dipole trap. This allows gravity to pull the atoms towards the $-\hat{z}$ direction while the random momentum of the atoms in the trap results in the cloud expanding in all directions. Along with gravity, $\mathbf{F}_{\mathrm{SG}}$ is an additional force in $\hat{z}$ which separates the clouds depending on their state. After allowing the atoms to separate over the course of $\sim$15 ms, a resonant imaging beam is shone at the atoms, and their shadow is cast on a CCD camera. This geometry is shown in figure 3.1b.

In order to produce an absorption image of the atomic cloud, the apparatus uses the same cycling transition from $|F = 2, m_F = 2\rangle$ to $|F' = 3, m_{F'} = 3\rangle$ that is used for optical pumping in state preparation. The use of a cycling transition means that the same atom can be involved in absorbing several photons of the same wavelength because after absorption the atom returns to its initial state, which produces a consistent level of absorption for imaging.

So far we have spatially separated clouds of atoms based on their $m_F g_F$ product and taken an absorption image of their positions. Ultimately, the

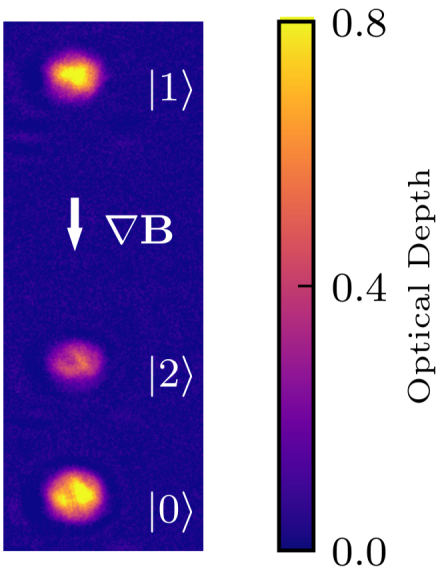

Figure 3.3: Typical readout image after processing. Optical depth is the log of the beam absorption, OD = $\log \frac{I_0}{I}$. The image is oriented vertically, with both gravity and the magnetic field gradient facing downwards. In this image, there is substantial population in each of the three qutrit states. They are split proportionally to $g_F m_F$, as shown by eq. (3.1), with $g_F m_F$ of states $|0\rangle$, $|1\rangle$, and $|2\rangle$ of 1, $-\frac{1}{2}$, and $+\frac{1}{2}$, respectively (see figure 2.3).

goal of state-readout is to determine the relative population of atoms in each cloud. After the atoms have fallen away, we take two more images. The first uses the same imaging beam power as the atom image, and the second absorbs only background light and noise. We can then calculate the absorption in the imaging-plane area A of each pixel,

$$\frac{I_0}{I} = \frac{V_0 - V_b}{V - V_b} \tag{3.2}$$

where I_0 and I are the incoming light intensity on the atom and the light intensity passing through the atoms, and V_0, V, V_b are the CCD readings of the pixel with the imaging beam turned on, with the imaging beam and the cloud of atoms, and with only background. From Beer's law, we find the optical depth is directly proportional to the atomic density n, [29]

$$\begin{aligned} \frac{dI}{dz} &= -n(x,y,z)\sigma(\omega)I \\ \log(I) - \log(I_0) &= -\sigma(\omega)\int_{-\infty}^{\infty} n(x,y,z)dz, \end{aligned} \tag{3.3}$$

where $\sigma(\omega)$ is the scattering cross section at the frequency ω [70]. Integrating across the pixel area,

$$\begin{aligned} \log \frac{I_0}{I} \iint_A dA &= \sigma(\omega) \int_{-\infty}^{\infty} \iint_A n(x,y,z) dA dz \\ \log \frac{V_0 - V_b}{V - V_b} A &= \sigma(\omega) N \end{aligned} \tag{3.4}$$

where N is the number of atoms imaged in the pixel area A. Thus the number of atoms in the a cloud can be counted by summing N for each pixel. With the sum total of N for each of the three clouds, we can calculate the relative populations. We call the term $\log \frac{I_0}{I}$ the *optical depth*. A processed image showing the optical depth distribution of a split cloud of atoms is shown in figure 3.3.

3.2 Calibration of Operators

Calibration of quantum processors is not a trivial task. As discussed in section 2.1.3, unitary operations are inherently continuous and error-prone. Even if quantum processors are successfully scaled up and run error correction algorithms, the native gates on physical qubits need excellent calibration. For example, the highest acceptable physical error rate may be around 1% for some architectures [30]. The uncharacterized and transient background magnetic field in our lab makes calibration yet more difficult.

3.2.1 Finding Resonance

Starting from an un-calibrated processor with a functional cooling and trapping sequence, the first step in gate calibration is to set the bias field B_0 and find the resonance frequencies $\omega_A = (E_{|0\rangle} - E_{|1\rangle})/\hbar$ and $\omega_B = (E_{|2\rangle} - E_{|1\rangle})/\hbar$. Generally, the bias magnetic field amplitude is set by external bias coils such that $\omega_z = g_F \mu_B B_0/\hbar \approx 1.25\,\mathrm{MHz}$, which requires a field of $\approx 1.8\,\mathrm{G}$. In practice, the $\hat{z}$ axis defining the qubit is approximately aligned with the $\hat{y}$ axis of the system as defined in figure 3.1b. Directly before imaging the field is adiabatically ramped towards the figure 3.1b z-axis so that the Stern-Gerlach force splits along the correct axis.

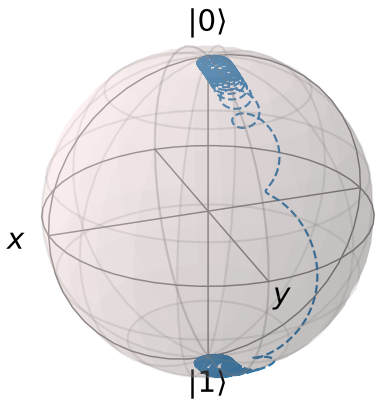

Figure 3.4: Evolution of a quantum state during an adiabatic rapid passage (ARP) sequence. The dotted-line trajectory of the state evolution. In this example simulation, the detuning is swept from 20Ω to -20Ω over a duration $T \approx 15/\Omega$, bringing the state from $|0\rangle$ to $|1\rangle$.

Since we cannot be sure what the real magnetic field is at the trap location, we use adiabatic rapid passage (ARP) [1] to find the resonance between the prepared initial state $|0\rangle$ and state $|1\rangle$. We begin by setting the background magnetic field bias coils to produce a field predominantly in the $\hat{y}$ direction. We find the resonance of the atoms by sending a slow, linearly chirped pulse across a wide frequency range. Assuming the pulse sweeps across the atomic resonance by starting and ending at very high detuning, the atoms will be transferred to $|1\rangle$. The mechanism can be visualized well on the Bloch sphere, and is shown in figure 3.4. Once a chirped frequency range is found that transfers population from $|0\rangle$ to $|1\rangle$, the resonance frequency can be found by bisection, narrowing the chirped range iteratively. Once the transition frequency for A was found, the transition frequency for B could be estimated, assuming linear Zeeman splitting, $\omega_B - \omega_{\mathrm{HF}} \approx \frac{2}{3}(\omega_A - \omega_{\mathrm{HF}})$.

In practice, once the approximate resonance is known, it was convenient to keep using the same resonance frequencies for transitions A and B, so the magnetic field bias was adjusted when necessary instead of the frequencies. If significant changes to the bias were necessary to find resonance, ARP could

still be used by sweeping the magnetic field bias instead of the frequency.

3.2.2 Magnetic field drift and noise

As is discussed in section 3.2.3, our system achieved Rabi frequencies of $|\Omega_A| \approx 2\pi \cdot 8\,\mathrm{kHz}$, making the total gate sequence including state preparation and readout approximately 600 µs. A detuning over $0.1|\Omega|$ would result in significant loss of performance. With a ≈1.8 G field, that means the stability should be better than 0.2 G. For perspective, the magnetic field of the Earth at the University of Alberta is approximately 0.5 G with a north-south component (roughly along the bias) of 0.15 G [55].

Our lab is subject to many sources of external magnetic field noise which are difficult to characterize. Notable among these are 60 Hz power line noise, instrumentation noise, and other nearby experiments.

To decrease sensitivity to 60 Hz noise, the experiment's microwave sequence is triggered by the power line cycle. This mechanism is not fully characterized, so we do not know how repeatable the power line triggering is from one experimental sequence to the next. We manually adjust a delay between the power line trigger and the start of the experimental sequence, trying to minimize the drift in experimental results. We expect this is optimizing the start of the cycle for the time when the magnetic field is near a peak or valley, so its derivative is instantaneously near zero.

Our lab is host to many instruments, including many power supplies, amplifiers, sensors, and lasers. Our main anti-Helmholtz coils, while they are nominally not passing any current during the microwave sequence, have a large power supply which produces nearly 400 A during the cooling sequence, and is connected to a large set of coils that could easily produce small fields from residual current. There are a total of 6 sets of coils near the atoms, any of which could produce small fields or RF noise to disturb the state of the atoms (bias coils for X, Y, Z, two sets of RF coils, and the anti-Helmholtz coils). Because of noise from instrumentation, we have had to move control electronics for the optical dipole trap acousto-optic modulators (AOMs) a few

metres further from the experiment than they were first positioned. While we have not identified a similar issue from lab equipment affecting the microwave sequence, any device emitting frequencies near $\omega_z \approx 2\pi \cdot 1.25\,\mathrm{MHz}$ or $\omega_{\mathrm{HF}} \approx 2\pi \cdot 6.83\,\mathrm{GHz}$ could affect the state of the atoms while being subtle enough for us not to notice.

In addition to our equipment, the experimental apparatus is surrounded by backgrounds from its neighbouring experiments. Frequently, our data was taken while the *Quantum memory* team, whose apparatus is located directly next to ours in the same lab, was running their equipment. Additionally, across the hallway, another group operated a 9 T magnet. We did not correlate any effect from their magnet's ramp-up and ramp-down sequence on our atomic cooling.

Qualitatively, the most noticeable background source was the 60 Hz power line. Because the compensation mechanism was synchronization, this means we could expect our bias to drift over the course of its 17 ms period. A total microwave sequence of 600 µs would occur within roughly 3.5% of a period.

3.2.3 Rabi frequency

Once the resonant frequencies for both transitions are found and the magnetic field bias was set, the next step is to characterize the Rabi frequencies. Recall from section 2.3.3, the dual-tone operator requires precise control of $\frac{\Omega_A}{\Omega_B}$ while $|\Omega_A|^2 + |\Omega_B|^2$ is fixed. The result is that the operator requires the Rabi frequencies $|\Omega_A|$ and $|\Omega_B|$ both to be well characterized such that their combination can be well targetted. We know $|\Omega| \propto |B_0|$ from eq. (2.20), and $|B_0| \propto \sqrt{P}$ where P is the power.

Figure 3.5a shows a recorded power spectrum from the intermediate-frequency input to the mixer when the AWG is outputting a continuous-wave dual-tone signal with equal amplitudes at 101.248 MHz and 103.73 MHz. Note the image sidebands are present in the spectrum but are suppressed by roughly 50 dB. The amplified spectrum after mixing is shown in figure 3.5b.

The sideband peaks of the amplified spectrum are suppressed by approxi-

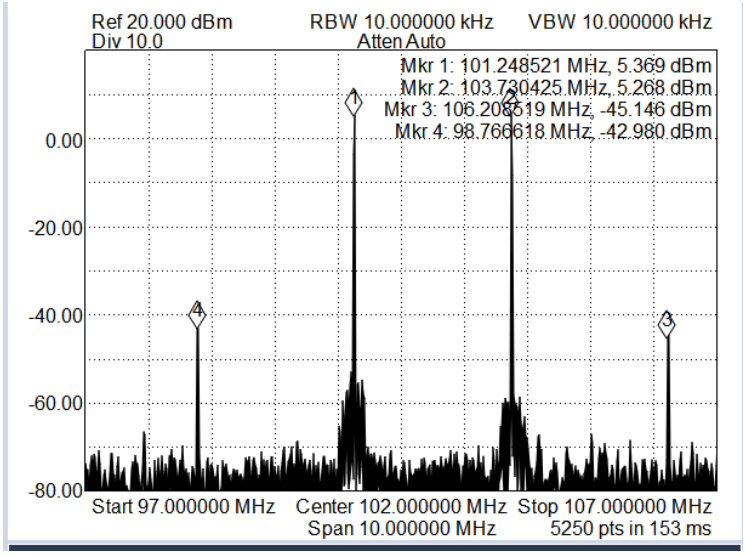

(a)

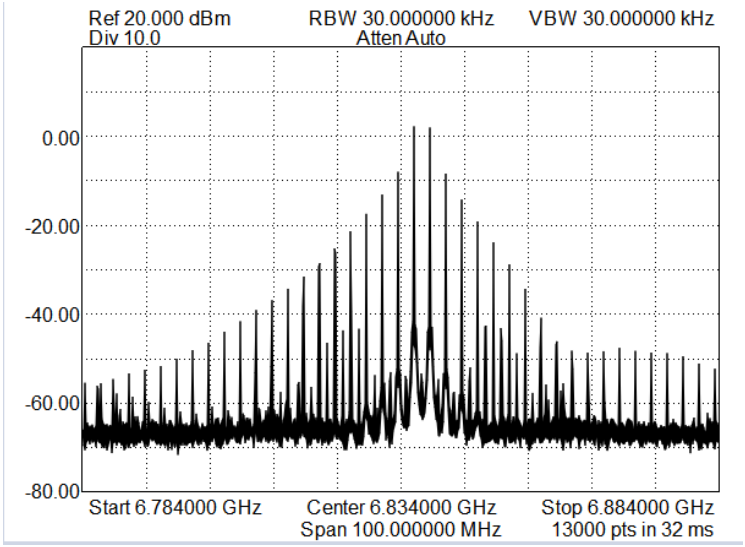

(b)

Figure 3.5: Dual-tone power spectra. Note the measurements were taken through attenuating directional couplers, so the figures provide relative power between peaks, but not an absolute power measurement. (a) the pre-amplified spectrum at the IF mixer port with equal power to two tones. (b) a wide spectrum coupled from the output of the amplifier.

mately 10 dB. In the amplified spectrum, when two tones are generated each with 300 $\mathrm{mV_{pp}}$ in the AWG, their amplitude is similar to driving a single tone with 85 $\mathrm{mV_{pp}}$. This significant reduction likely results from a combination of sidebands and amplifier saturation at the significantly higher power level. It would be convenient to operate the amplifier significantly below saturation, where microwave tones could be added roughly linearly. Unfortunately, our microwave system is significantly Rabi-frequency-constrained, so maximizing the possible Rabi frequency is a higher priority than operating the amplifier in a linear regime. As a result, to perform a dual-tone operation, the relative amplitudes of each tone and the duration of the operation required were set manually by adjusting the parameters until the final state fidelity was optimized for each input basis state.

At the start of an experiment, the atoms are in state $|0\rangle$, prepared by optical pumping. If we wished to apply an operator from the starting state $|1\rangle$, a resonant π-area pulse was applied before the rest of the microwave sequence. This completed in roughly 75 µs. To prepare state $|2\rangle$, a second π-area pulse, resonant with transition B, is applied after the pulse to $|1\rangle$, adding an additional 60 µs for state preparation. In order to ensure an operator to be tested experiences the same background magnetic field (synchronized to the 60 Hz line), experiments on state $|0\rangle$ started with a 135 µs "no-op" operation, which was used to fill the gap that would have otherwise been used for state preparation. Additionally, since transients in the amplifier or the amplifier's power supply were suspected of causing the Rabi frequency to change as a function of pulse duration, the "no-op" was not a blank sequence, but a pulse of a frequency far-detuned from any atomic transitions.

Figure 3.6 shows a long-duration Rabi scan measured on the system between states $|1\rangle$ and $|2\rangle$. The top subplot shows a measured Rabi frequency of approximately $2\pi \cdot 8.2$ kHz. Before this scan, a π-area pulse was used for state preparation. A potential transient in the amplifier's output would affect the preparation pulse, and not the main Rabi scan displayed here. There is one outlier point near 0.5 ms which has all atoms detected in state $|0\rangle$. This is a

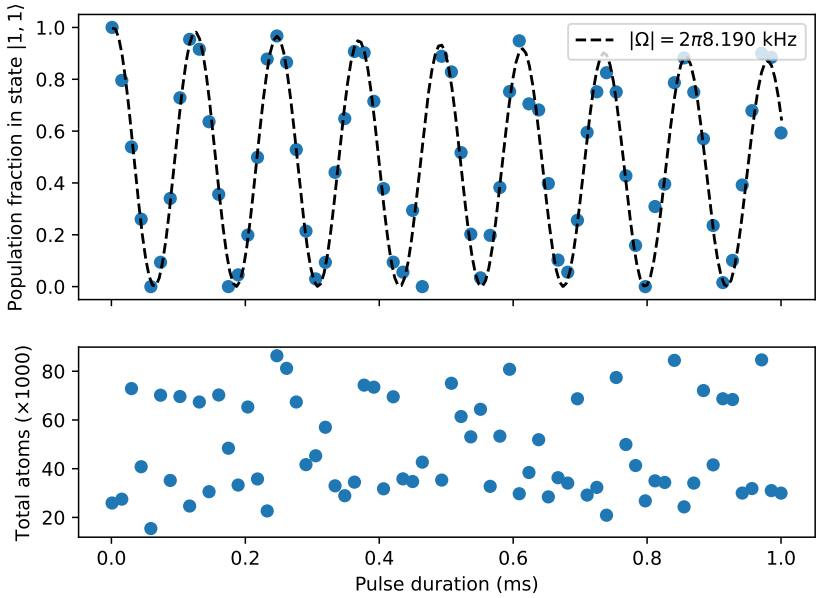

Figure 3.6: Long-duration Rabi scan between states $|1\rangle$ and $|2\rangle$, showing the cloud fraction in state $|1\rangle$ and the total number of atoms measured.

common indication of a missed trigger by the arbitrary waveform generator, which can occur if the waveform generator is not ready for triggering before the atom cooling process is complete. The bottom subplot shows the total number of atoms detected across all clouds. Note the significant noise in the total atom number which indicates significant instability in the atomic cooling and trapping from one shot to the next.

Because Rabi frequencies were difficult to characterize, pulse areas were set by optimizing the ending populations in each of the clouds when the operator is applied on top of each input state.

3.3 Experiment concept

Control over the atomic ensemble qutrit was tested by checking the final state fidelity when applying the quantum Fourier transform to each computational basis state. The quantum Fourier transform was created by two methods: single-tone SU(2) rotations, and a dual-tone decomposition.

3.3.1 The Quantum Fourier Transform

The quantum Fourier transform for a qutrit is

$$\hat{F} = \frac{1}{\sqrt{3}} \begin{pmatrix} 1 & 1 & 1 \\ 1 & e^{i\frac{2\pi}{3}} & e^{-i\frac{2\pi}{3}} \\ 1 & e^{-i\frac{2\pi}{3}} & e^{i\frac{2\pi}{3}} \end{pmatrix}. \tag{3.5}$$

The operator is also known as the Walsh-Hadamard gate [81] as it is an extension of the Hadamard transform in qubits [41] – it maps eigenstates to equal superpositions with a natural phase offset. The gate has wide applications including Shor's algorithm [74], error correction [81], and the Bernstein-Vazirani algorithm [78]. Because it is a non-trivial and important single-qutrit operation, it was chosen as a demonstrator of the universal single-qutrit control available using the ^{87}Rb system.

We performed the single-qutrit quantum Fourier transform using two operator decompositions – one using conventional single-tone SU(2) rotations and a second incorporating the dual-tone operator to indirectly couple states $|0\rangle$ and $|2\rangle$. The operators were applied to each of the computational basis states, and the final state was determined by quantum state tomography. The results are described in section 4.6.

Chapter 4

Complete Unitary Qutrit Control in Ultracold Atoms

This chapter contains a full reproduction of *Complete Unitary Qutrit Control in Ultracold Atoms*, [45]. As discussed in the preface, this paper was co-authored with Dr. Arina Tashchilina, Dr. Logan W. Cooke, and Dr. Lindsay J. LeBlanc. While I wrote the first draft of the paper, many improvements were made with the help of my co-authors. Figures 4.1, 4.2(a,c), and 4.4 were all created by Dr. LeBlanc.

4.1 Abstract

Physical quantum systems are commonly composed of more than two levels and offer the capacity to encode information in higher-dimensional spaces beyond the qubit, starting with the three-level qutrit. Here, we encode neutral-atom qutrits in an ensemble of ultracold ^{87}Rb and demonstrate arbitrary single-qutrit SU(3) gates. We generate a full set of gates using only two resonant microwave tones, including synthesizing a gate that effects a coupling between the two disconnected levels in the three-level Λ-scheme. Using two different gate sets, we implement and characterize the Walsh-Hadamard Fourier transform, and find similar final-state fidelity and purity from both approaches. This work establishes the ultracold neutral-atom qutrit as a promising platform for qutrit-based quantum information processing, extentions to d-dimensional qudits, and explorations in multilevel quantum state manipula-

tions with nontrivial geometric phases.

4.2 Introduction

The conventional paradigm for universal quantum computing makes use of two-level qubits, but higher-dimensional quantum systems offer considerable advantages. Logical operations and information storage using three-level systems – "qutrits" – in a larger Hilbert space give way to algorithms that can be more efficient [78] and allow for more complex entanglement than qubits [17]. Qutrits [25] and higher d-dimensional qudits [32] are valuable as a quantum resources for speed-up and for improved cryptographic security in transmission over quantum networks [14, 38, 53]. Additionally, using a third temporary-state level during the implementation of a qubit gate can significantly improve fidelities and reduce circuit complexity [12, 34, 38, 44].

While qubits are readily simulated by the polarization of classical light, qutrits offer an additional complexity that reflects their inherently quantum properties [25]. Many physical platforms have served as host to qutrits [41, 51, 78], including photonic systems [4, 13, 27, 43, 47, 53, 69], NMR ensembles [25], superconducting quantum circuits [9, 10, 21, 42, 54, 81], and trapped ions [5, 41, 46, 65, 67]. In contrast to qubit operations, single *qutrit* gates are represented by 3×3 unitary matrices in the group SU(3), generated by the eight Gell-Mann matrices $\hat{\lambda}_i$ [17]. Experimental qutrit demonstrations to date realized arbitrary operations by decomposing the desired transformation into three SU(2) operations followed by a diagonal phase gate [41, 42, 74, 81]. In many physical systems, two of the three SU(2) couplings are accessible, but selection rules dictated by parity mean that the third is less convenient or even forbidden. To overcome this, two resonant couplings on the accessible transitions can be combined as a simultaneous dual-tone operator to synthesize the third coupling [41].

In this work, we demonstrate neutral-atom qutrits in ultracold ensembles, taking advantage of the well-defined, long-lived, and readily controlled hyper-

fine transitions in the alkali metals. We synthesize arbitary single-qutrit gates using two different schemes, both of which require only two couplings in the three-state manifold (Fig. 4.1). In one of these approaches [41], we show an effective coupling between two levels that are not simply connected by microwave fields, establishing a comprehensive set of two-state operations within the three-state manifold. Our work specifically isolates and controls individual couplings within a qutrit with simple unitary decompositions that can be applied, in principle, to other qutrit platforms. This work builds beyond previous experiments [2, 18] which use highly-parameterized control waveforms and gradient ascent to effect a target unitary on the space of one or more hyperfine manifolds. Ensemble systems like ours provide a testbed for general quantum information processing with atoms [6, 68], though progress in atom-based quantum information processing with neutral-atom arrays [11, 35, 58, 68] is rapidly advancing. Adapting the ensemble approach described here to address individual atoms could be achieved through site-specific gradients, focussed light shifts, or phase control [71, 75–77], opening up the advantages of qutrits across atomic quantum computing platforms. More broadly, the approach to quantum state control demonstrated here will provide tools for exploring fundamental operations on multilevel systems, including engineering nontrivial geometric phases in atomic systems [19, 56, 72].

4.3 Single qutrit gates.

A qutrit $|\psi\rangle = \sum_{k=0}^{2} c_k e^{i\phi_k} \,|\, k \,\rangle$ is defined by the parameters $\{c_k\}$ and $\{\phi_k\}$, four of which are independent after considering normalization and global phase invariance. A single-qutrit gate, part of SU(3), is defined by eight independent parameters [74]. In a system with only two (complex) couplings [Fig. 4.1(a)], sequential operations can be applied to span all eight parameters, followed by a two-parameter relative phase adjustment, $\hat{U}_\theta(\eta, \epsilon)$. In one approach [25, 42, 54], a general single-qutrit gate is implemented with single-tone operators,

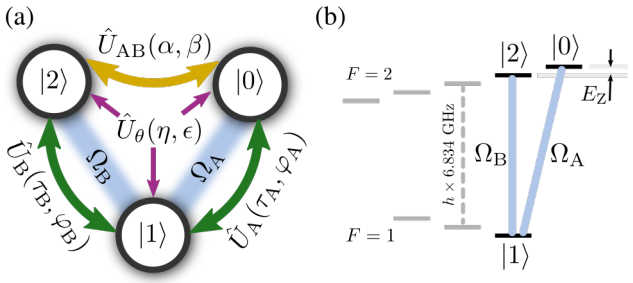

Figure 4.1: (a) Schematic representation the three qutrit levels $\{|\,0\,\rangle, |\,1\,\rangle, |\,2\,\rangle\}$, where direct couplings (Ω_{A} and Ω_{B}) exist only between $|\,0\,\rangle \leftrightarrow |\,1\,\rangle$ and $|\,1\,\rangle \leftrightarrow |\,2\,\rangle$, and are associated with unitary operations $\hat{U}_{\mathrm{A}}$ and $\hat{U}_{\mathrm{B}}$. With a dual-tone operator, coupling between $|\,0\,\rangle \leftrightarrow |\,2\,\rangle$ is possible via $\hat{U}_{\mathrm{AB}}$; an additional phase-only operator $\hat{U}_{\theta}$ can be applied across all levels. (b) Energy level diagram of the ^{87}Rb ground-state manifold, with levels $|\,0\,\rangle \rightarrow |\,F=2, m_F=2\,\rangle$, $|\,1\,\rangle \rightarrow |\,F=1, m_F=1\,\rangle$, and $|\,2\,\rangle \rightarrow |\,F=2, m_F=1\,\rangle$ connected by two magnetic dipole transitions at microwave frequencies, whose energy difference is controlled by the Zeeman splitting, E_{Z}.

such as

$$\hat{U}^{\mathrm{I}}_{\mathrm{gen.}} = \hat{U}_{\theta}(\eta,\epsilon)\hat{U}_{\mathrm{B}}(\chi_{\mathrm{B2}},\varphi_{\mathrm{B2}})\hat{U}_{\mathrm{A}}(\chi_{\mathrm{A1}},\varphi_{\mathrm{A1}})\hat{U}_{\mathrm{B}}(\chi_{\mathrm{B1}},\varphi_{\mathrm{B1}}), \tag{4.1}$$

where $\chi_{\mathrm{Xi}} = |\Omega_{\mathrm{X}}|t/2$ and $\varphi_{\mathrm{Xi}} = \arg(\Omega_{\mathrm{X}})$ are the pulse areas and coupling phases for transitions $\mathrm{X} = \{\mathrm{A},\mathrm{B}\}$ with parameter index i, and $\{\eta,\epsilon\}$ are relative phase adjustments (see Section 4.8).

In a second approach [41], (sec. 4.8), a dual-tone operator is used to simultaneously drive both transitions A and B to synthesize a third coupling $\hat{U}_{\mathrm{AB}}(\chi_{\mathrm{AB}},\varphi_{\mathrm{AB}})$ between states $|\,0\,\rangle \leftrightarrow |\,2\,\rangle$, where the operator duration is exactly $t_{\mathrm{AB}} = 2\pi/\sqrt{|\Omega_{\mathrm{A}}|^2 + |\Omega_{\mathrm{B}}|^2}$ and the parameters χ_{AB} and φ_{AB} are derived from the complex couplings $\Omega_{\mathrm{A,B}}$ (sec. 4.8). A general gate is implemented through a combination of operators such as

$$\hat{U}^{\mathrm{II}}_{\mathrm{gen.}} = \hat{U}_{\theta}(\eta,\epsilon)\hat{U}_{\mathrm{B}}(\chi_{\mathrm{B2}},\varphi_{\mathrm{B2}})\hat{U}_{\mathrm{A}}(\chi_{\mathrm{A1}},\varphi_{\mathrm{A1}})\hat{U}_{\mathrm{AB}}(\chi_{\mathrm{AB}},\varphi_{\mathrm{AB}}). \tag{4.2}$$

In both decompositions I and II, the first SU(2) operator $\hat{U}_{\mathrm{AB,B}}$ is designed such that $\hat{U}_{\mathrm{gen.}}\hat{U}^{\dagger}_{\mathrm{AB,B}}$ has one off-diagonal matrix element of zero. The second pulse $\hat{U}_{\mathrm{A}}$ zeroes three more off-diagonal matrix elements in $\hat{U}_{\mathrm{gen.}}\hat{U}^{\dagger}_{\mathrm{AB,B}}\hat{U}^{\dagger}_{\mathrm{A}}$, and

after the third only a diagonal phase remains which is implemented by $\hat{U}_\theta$ (see sec. 4.8).

As a particular example of a single-qutrit gate that uses control over all eight parameters, we consider the Walsh-Hadamard gate, which is the single-qutrit Fourier transform [41],

$$\hat{F} = \frac{1}{\sqrt{3}} \begin{pmatrix} 1 & 1 & 1 \\ 1 & e^{i\frac{2\pi}{3}} & e^{-i\frac{2\pi}{3}} \\ 1 & e^{-i\frac{2\pi}{3}} & e^{i\frac{2\pi}{3}} \end{pmatrix}. \tag{4.3}$$

This transform has broad applications, such as Shor's algorithm [74], error correction [81], implementing the SWAP gate, and the Bernstein-Vazirani algorithm [78]. In the single- and dual-tone operator decompositions described above, the Fourier transforms are implemented as

$$\hat{F}^{\mathrm{I}} = e^{i\pi/6}\hat{U}_\theta(-\tfrac{\pi}{6}, -\tfrac{\pi}{6})\hat{U}_{\mathrm{B}}\left(\tfrac{5\pi}{4}, \tfrac{\pi}{2}\right)\hat{U}_{\mathrm{A}}\left(\chi_{\mathrm{A}}^{\mathrm{I}}, \pi\right)\hat{U}_{\mathrm{B}}\left(\tfrac{\pi}{4}, 0\right), \tag{4.4}$$

$$\hat{F}^{\mathrm{II}} = i\hat{U}_\theta\left(\tfrac{\pi}{3}, -\tfrac{\pi}{2}\right)\hat{U}_{\mathrm{A}}\left(\tfrac{\pi}{4}, \tfrac{\pi}{6}\right)\hat{U}_{\mathrm{B}}\left(\chi_{\mathrm{B}}^{\mathrm{II}}, \tfrac{\pi}{3}\right)\hat{U}_{\mathrm{AB}}\left(\tfrac{\pi}{4}, -\tfrac{2\pi}{3}\right), \tag{4.5}$$

where $\chi_{\mathrm{A}}^{\mathrm{I}} = \arccos(-1/3)/2$ and $\chi_{\mathrm{B}}^{\mathrm{II}} = \pi + \arctan(1/\sqrt{2})$.

We implement both the single- and dual-tone Fourier transform operators to experimentally explore ultracold atomic ensembles as a platform for qutrit operations, and to compare the two approaches to qutrit operators in terms of final state fidelity and purity.

4.4 Experimental Methods

In our experiments, we prepare ultracold ensembles of ^{87}Rb atoms, manipulate the internal electronic states [Fig. 4.1(b)] using resonant microwave pulses, and measure the results by analyzing the final state via absorption imaging. The ensemble approach allows us to perform simultaneous experiments on a large number ($\sim 10^5$) of identical atoms using spatially uniform fields, and the measurement over the entire ensemble gives a statistical measure of the final state in a single experimental run. The atoms remain coherent for well over 1 ms, ensuring enough time to complete all operations in this protocol without dephasing or decoherence.

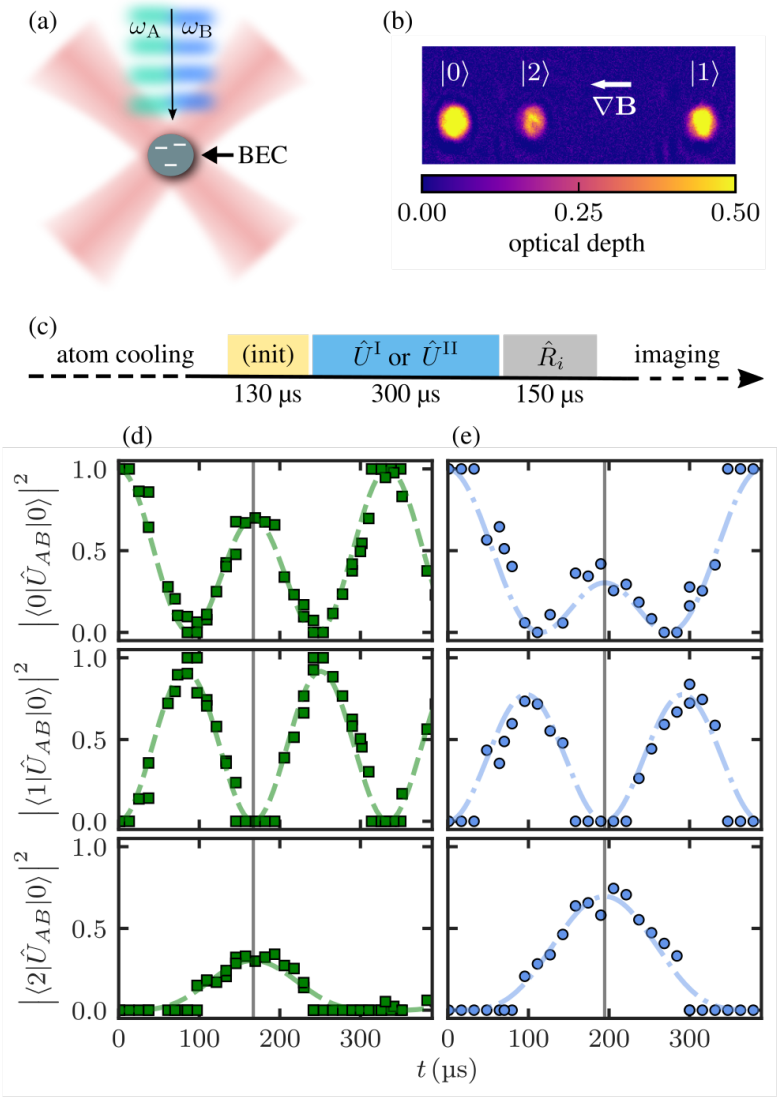

Figure 4.2: (a) A BEC of ^{87}Rb is trapped at the intersection of two optical dipole beams. Resonant microwave radiation with frequencies ω_A and/or ω_B drives transitions between levels. (b) A magnetic field gradient $\nabla\mathbf{B}$ is applied to the atoms during time-of-flight, before absorption imaging, spatially separating atomic levels according to their magnetic moments, μ_i, where $\mu(|0\rangle) = \mu_B$, $\mu(|1\rangle) = -\mu_B/2$, and $\mu(|2\rangle) = \mu_B/2$, and μ_B is the Bohr magneton. The colour map represents an absorption image after 25 ms time of flight, with color bar indicating the optical depth of the atoms in clouds associated with each level. (c) Timing sequence for cooling, state initialization, qutrit gates $\hat{U}^{I,II}$, and tomography rotations $\hat{R}_i$. (d,e) Example calibration data for dual-tone operators $\hat{U}_{AB}(0.19\pi, 0)$ in (d) and $\hat{U}_{AB}(0.31\pi, 0)$ in (e). Vertical gray lines indicate the operator time t_{AB} for which the intermediate-state $|1\rangle$ population/amplitude is zero.

In particular, we prepare 10^5 Bose-Einstein condensed ^{87}Rb atoms in an actively stabilized optical dipole trap. The ground $5^2S_{1/2}$ state of ^{87}Rb has two hyperfine levels, $F = 1$ and $F = 2$, separated by $\omega_{\rm HF} = 2\pi \times 6.835\,{\rm GHz}$, each of which hosts $2F+1$ Zeeman sub-levels, which are energetically split by $E_{\rm Z} \approx h \times 1.25\,{\rm MHz}$ in a weak magnetic field. Using optical pumping, we initialize all atoms in the spin-polarized input state $|\psi_{\rm in}\rangle = |\,0\,\rangle \equiv |\,F = 2, m_F = 2\,\rangle$. All microwave operations are triggered to begin at the same phase of a 60 Hz line oscillation. Optionally, we use π-pulse operations ($\hat{U}_{\rm A}$ or $\hat{U}_{\rm B}\hat{U}_{\rm A}$ pulses) to prepare initial states $|\,\psi_{\rm in}\,\rangle = |\,1\,\rangle$ or $|\,2\,\rangle$. In this work, we use only microwave couplings between states of different F to complete operations, avoiding the radiofrequency couplings between levels in the same F manifold, which would allow direct $|0\rangle$ to $|2\rangle$ coupling. By doing this, we avoid simultaneous couplings between all m_F states in that manifold, due to the degeneracy of the Zeeman transitions in a weak magnetic field. The microwave transitions we use are, in contrast, nondegenerate, even in weak magnetic fields.

Amplitude- and phase-controlled microwave signals, tuned near $\omega_{\rm HF}$, are resonant with the "A" $|\,0\,\rangle \leftrightarrow |\,1\,\rangle \equiv |\,F = 1, m_F = 1\,\rangle$ and "B" $|\,1\,\rangle \leftrightarrow |\,2\,\rangle \equiv |\,F = 2, m_F = 1\,\rangle$ transitions with typical Rabi frequencies $|\Omega_{\rm A,B}| \sim 2\pi\times 2\,{\rm kHz}$. These two microwave tones, timed appropriately, effect the unitary operations $\hat{U}_{\rm A}$ or $\hat{U}_{\rm B}$ when used alone, and $\hat{U}_{\rm AB}$ when driven together (see sec. 4.8). Figures 4.2(c,d) show the dual-tone operator $\hat{U}_{\rm AB}$ acting on initial state $|\,\psi_{\rm in}\,\rangle = |\,0\,\rangle$ for varying pulse times: at the operator time $t_{\rm AB}$, the results show the populations distributed between $|\,0\,\rangle$ and $|\,2\,\rangle$ only. This distribution is controlled by the parameters $\chi_{\rm AB}$ and $\varphi_{\rm AB}$, which themselves depend on the amplitudes and phases of $\Omega_{\rm A}$ and $\Omega_{\rm B}$.

To effect a general single-qutrit gate, up to three of these operators are applied to the system, along with relative phase control (see sec. 4.8). To decipher the amplitude and phase information of the resulting output state qutrits $|\,\psi_{\rm out}\,\rangle$, we perform tomography by applying rotation operations to the system (see below for details). After the operations are complete, the atoms are released from the trap and the populations $|c_i|^2$ of each level in

the qutrit are measured via absorption imaging: the three levels are spatially separated by a Stern-Gerlach magnetic field gradient in time-of-flight, and counted simultaneously in a single absorption image [Fig. 4.2(b)].

4.5 Tomography

To determine the full effect of the single-qutrit gates, we perform quantum state tomography on the final states $|\psi_{\rm out}\rangle$ for each of $\hat{U}^{\rm I}_{\rm gen}$ and $\hat{U}^{\rm II}_{\rm gen}$ acting on three orthogonal input states, $|\,\psi_{\rm in}\,\rangle = \{|\,0\,\rangle, |\,1\,\rangle, |\,2\,\rangle\}$. Eight linearly independent projections of the qutrit state are required to fully characterize its density matrix $\hat{\rho} = \frac{\hat{\mathbb{1}}}{3} + \frac{1}{3}\sum_{k=1}^{8}\langle\hat{\lambda}_k\rangle\hat{\lambda}_k$ [17].

To perform the tomography, read-out operators $\hat{R}_i$ (Table 4.1) are applied before projective measurement. Table 4.2 shows how the orthogonal Gell-Mann matrices can be constructed from these projections. The usual projection operation $\langle\psi_{\rm out}|\chi\rangle\langle\chi|\psi_{\rm out}\rangle$ extends to $\mathrm{Tr}(|\chi\rangle\langle\chi|\hat{\rho}_{\rm out})$ when a density matrix $\hat{\rho}_{\rm out}$ is substituted for the pure state $|\,\psi_{\rm out}\,\rangle$. We measure three projections for each of the six read-out operators, $\langle\hat{R}_i^\dagger|0\rangle\langle 0|\hat{R}_i\rangle$, $\langle\hat{R}_i^\dagger|1\rangle\langle 1|\hat{R}_i\rangle$, and $\langle\hat{R}_i^\dagger|2\rangle\langle 2|\hat{R}_i\rangle$, and in total, we measure 6×3 projections, which are not all linearly independent.

An iterative maximum likelihood technique [49] allows us to estimate the density matrix $\hat{\rho}$ while maintaining the condition $\mathrm{Tr}(\hat{\rho}) = 1$. Using the function

$$\hat{Q}(\hat{\rho}) = \sum_i \sum_{j=0,1,2} \frac{f_j^i}{\mathrm{Tr}\left(\hat{R}_i^\dagger|j\rangle\langle j|\hat{R}_i\hat{\rho}\right)} \hat{R}_i^\dagger|j\rangle\langle j|\hat{R}_i, \tag{4.6}$$

where f_j^i is the cloud fraction found experimentally in eigenstate $|j\rangle$ after the read-out operator $\hat{R}_i$ is applied, we iterate through

$$\hat{\rho}_{i+1} = \frac{\hat{Q}(\hat{\rho}_i)\hat{\rho}_i\hat{Q}(\hat{\rho}_i)}{\mathrm{Tr}\left(\hat{Q}(\hat{\rho}_i)\hat{\rho}_i\hat{Q}(\hat{\rho}_i)\right)} \tag{4.7}$$

until convergence, having begun with the maximally mixed density matrix $\hat{\rho}_0 = \hat{\mathbb{1}}/3$ (Ref. [17]).

Table 4.1: Read-out operators used for quantum state tomography. They are all $\pi/2$-area pulses.

$\hat{R}_i$	Basis	Phase ϕ	Matrix form
$\hat{R}_1$	$\{\|0\rangle, \|1\rangle\}$	0	$\frac{1}{\sqrt{2}}\begin{pmatrix} 1 & -1 & 0 \\ 1 & 1 & 0 \\ 0 & 0 & \sqrt{2} \end{pmatrix}$
$\hat{R}_2$	$\{\|0\rangle, \|1\rangle\}$	$\frac{\pi}{2}$	$\frac{1}{\sqrt{2}}\begin{pmatrix} 1 & -i & 0 \\ -i & 1 & 0 \\ 0 & 0 & \sqrt{2} \end{pmatrix}$
$\hat{R}_3$	$\{\|1\rangle, \|2\rangle\}$	0	$\frac{1}{\sqrt{2}}\begin{pmatrix} \sqrt{2} & 0 & 0 \\ 0 & 1 & 1 \\ 0 & -1 & 1 \end{pmatrix}$
$\hat{R}_4$	$\{\|1\rangle, \|2\rangle\}$	$\frac{\pi}{2}$	$\frac{1}{\sqrt{2}}\begin{pmatrix} \sqrt{2} & 0 & 0 \\ 0 & 1 & -i \\ 0 & -i & 1 \end{pmatrix}$
$\hat{R}_5$	$\{\|0\rangle, \|2\rangle\}$	0	$\frac{1}{\sqrt{2}}\begin{pmatrix} 1 & 0 & -1 \\ 0 & -\sqrt{2} & 0 \\ -1 & 0 & -1 \end{pmatrix}$
$\hat{R}_6$	$\{\|0\rangle, \|2\rangle\}$	$\frac{\pi}{2}$	$\frac{1}{\sqrt{2}}\begin{pmatrix} 1 & 0 & -i \\ 0 & -\sqrt{2} & 0 \\ i & 0 & -1 \end{pmatrix}$

Table 4.2: Demonstration of the Gell-Mann matrices constructed using read-out operators $\hat{R}_i$.

$\hat{\lambda}_i$	Construction
$\hat{\lambda}_1$	$\hat{R}_1^\dagger \left(\|1\rangle\langle 1\| - \|0\rangle\langle 0\|\right) \hat{R}_1$
$\hat{\lambda}_2$	$\hat{R}_2^\dagger \left(\|0\rangle\langle 0\| - \|1\rangle\langle 1\|\right) \hat{R}_2$
$\hat{\lambda}_3$	$\hat{R}_3^\dagger \|2\rangle\langle 2\| \hat{R}_3 - \hat{R}_5^\dagger \|1\rangle\langle 1\| \hat{R}_5$[1]
$\hat{\lambda}_4$	$\hat{R}_5^\dagger \left(\|2\rangle\langle 2\| - \|0\rangle\langle 0\|\right) \hat{R}_5$
$\hat{\lambda}_5$	$\hat{R}_6^\dagger \left(\|0\rangle\langle 0\| - \|2\rangle\langle 2\|\right) \hat{R}_6$
$\hat{\lambda}_6$	$\hat{R}_3^\dagger \left(\|1\rangle\langle 1\| - \|2\rangle\langle 2\|\right) \hat{R}_3$
$\hat{\lambda}_7$	$\hat{R}_4^\dagger \left(\|1\rangle\langle 1\| - \|2\rangle\langle 2\|\right) \hat{R}_4$
$\hat{\lambda}_8$	$\left(\hat{R}_3^\dagger \|0\rangle\langle 0\| \hat{R}_3 + \hat{R}_5^\dagger \|1\rangle\langle 1\| \hat{R}_5 - 2\hat{R}_1^\dagger \|2\rangle\langle 2\| \hat{R}_1\right)/\sqrt{3}$[2]

[1] One of 4 possibilities shown

[2] One of 8 possibilities shown

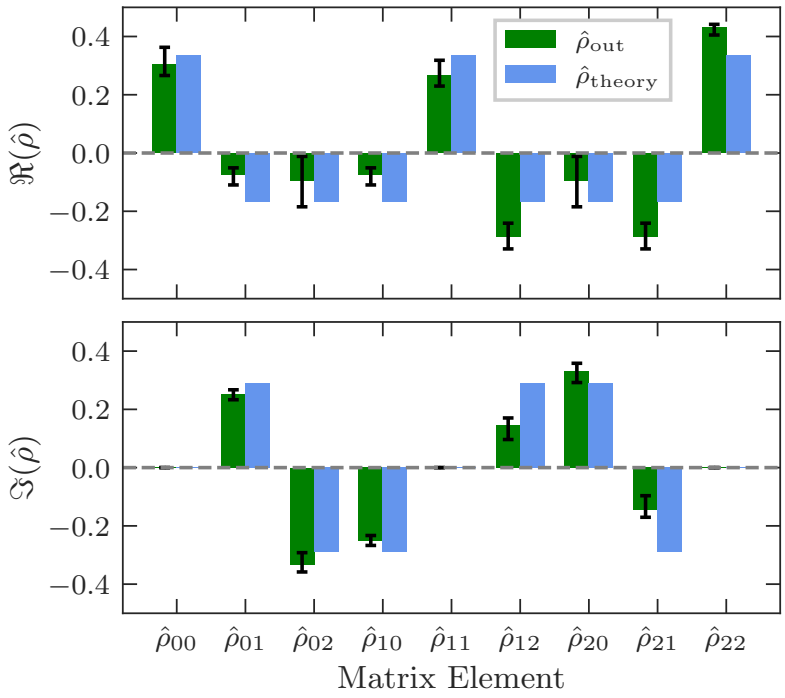

Figure 4.3: Reconstructed density matrix elements from the measured values $\hat{\rho}_{\text{out}}$ (green, left bars) and for the modelled, expected density matrix $\hat{\rho}_{\text{theory}}$ (blue, right bars) for the Fourier operation $\hat{F}^{\text{II}}\,|0\rangle$. The real (upper) $\Re(\hat{\rho})$ and imaginary (lower) $\Im(\hat{\rho})$ parts of these elements are shown. Error bars show the range of each matrix element across all $N = 10$ tomographic measurements. As a Hermitian operator, the main diagonal of $\hat{\rho}$ is real.

Table 4.3: Fidelity and purity found by maximum likelihood estimation after state tomography for two decompositions of the single-qutrit Fourier transform. Errors shown are the standard deviation of values across the N tomographic measurements. State preparation and measurement errors are not removed.

Operator	$\|\psi_{\text{in}}\rangle$	N	$\mathcal{P}$	$\mathcal{F}$	$\mathcal{F}_{\text{pure}}$
$\hat{F}^{II}$	$\|0\rangle$	10	0.93(4)	0.91(2)	0.95(2)
	$\|1\rangle$	10	0.92(3)	0.91(2)	0.96(2)
	$\|2\rangle$	10	0.90(6)	0.86(4)	0.92(2)
$\hat{F}^{I}$	$\|0\rangle$	15	0.90(8)	0.92(6)	0.98(3)
	$\|1\rangle$	12	0.88(8)	0.87(5)	0.95(3)
	$\|2\rangle$	16	0.89(4)	0.89(7)	0.95(7)

4.6 Results

We applied the Walsh-Hadamard decompositions $\hat{F}^{\text{I}}$ and $\hat{F}^{\text{II}}$ on three input computational basis states $|0\rangle$, $|1\rangle$, and $|2\rangle$ and characterize the output state's density matrix, $\hat{\rho}_{\text{out}}$. Figure 4.3 shows one such density-matrix reconstruction, after applying $\hat{F}^{\text{II}}$ to the state $|0\rangle$. For each tomographically measured $\hat{\rho}_{\text{out}}$ (resulting from one of $\hat{F}^{\text{I,II}}$ acting on an input basis state $|\,n\,\rangle$), we calculate the quantum state fidelity [39]

$$\mathcal{F}(\hat{F}, |\,n\,\rangle) = \langle n|\hat{F}^{\dagger}\hat{\rho}_{\text{out}}\hat{F}|n\rangle \tag{4.8}$$

and purity $\mathcal{P}(\hat{\rho}_{\text{out}}) = \text{Tr}(\hat{\rho}^2_{\text{out}})$. Table 4.3 shows that the single qutrit gates operate as expected for all input basis states, and that the two decompositions produce states with similar fidelities and purities.

The ensemble approach taken in this work gives excellent statistics and provides a fast path towards calibrating the pulse areas and phases. However, this approach is not without its limitations, which we see in the values for both the fidelity $\mathcal{F}$ and purity $\mathcal{P}$. After averaging each measurement over $N \geq 10$ experimental trials [Fig. 4.4], we find that variations in the results decrease with increasing N, but the average values remain similar to the single $N = 1$ trial. This indicates that shot-to-shot noise is not a significant contributor to the infidelity and impurity of these measures. In contrast, we find that the impurity of the final states impacts the fidelity: if we assume the nearest pure

state is achieved before calculating the fidelity using Eq. 4.8 by estimating that state as

$$\hat{\rho} \to \frac{\hat{\rho} - \hat{\mathbb{1}}/3}{\mathcal{P}(\hat{\rho})} + \frac{\hat{\mathbb{1}}}{3}. \tag{4.9}$$

we find better $\mathcal{F}_{\text{pure}}$ than $\mathcal{F}$, indicating that a significant part of the infidelity arises from loss of purity. Spatial inhomogeneities in the coupling fields or the environment experienced by atoms may cause position-dependent evolution and appear as a loss of ensemble purity. Our analysis (see sec. 4.8) suggests the dominant effect is dephasing of the qutrit due to Stark-shift inhomogeneity in the optical dipole trap: atoms in the centre of the trap have a detuning on the order of 400 Hz relative to those at the edges, and because the atoms are cold and move little during the operation time, this difference does not average out over the course of a gate sequence. A probable source of the the remaining infidelity is imprecision in the calibration of individual operators.

4.7 Discussion

We successfully demonstrated arbitrary SU(3) control in neutral alkali atoms using the Walsh-Hadamard (Fourier transform) single-qutrit gate, while implementing the resonant dual-tone operator $\hat{U}_{\text{AB}}$. We find that two different decompositions of arbitrary SU(3) gates using three SU(2) rotations result in comparable fidelities. The dual-tone operator $\hat{U}_{\text{AB}}$ is particularly useful for qutrit operations in platforms where one coupling is forbidden or inconvenient to use, not only in the ultracold atomic states used here, but also in systems such as superconducting qutrits [81] and ions [41]. In our experiments, for example, we harnessed U_{AB} to perform each tomographic read-out operation in a single step, while previous works [9, 81] have needed several pulses to prepare some projections.

When decomposing SU(d) operations into SU(2) steps, the number of operations scales quadratically with d. In the future, alternative approaches to SU(3) operations could be implemented by decomposing via Householder reflections rather than SU(2) operations, which scales linearly with d by applying

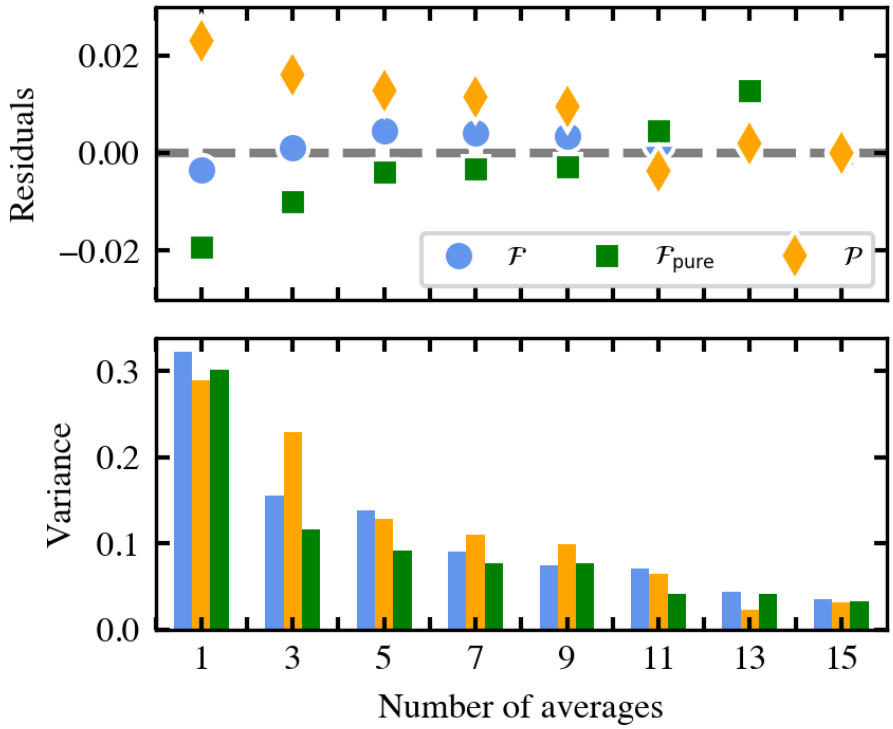

Figure 4.4: Gate quality metrics $\mathcal{F}$, $\mathcal{P}$, and $\mathcal{F}_{\text{pure}}$ after averaging over N experimental scans. The upper plot shows the residuals for results with respect to the average over $N = 15$ scans, and the lower plot shows the variance of the results (given as the variance between the maximum and the minimum of each metric): left blue bars: $\mathcal{F}$, middle yellow bars: $\mathcal{P}$, right green bars: $\mathcal{F}_{\text{pure}}$. While the variance reduces with more averaging, as expected, there is minimal change in the average value (seen via the residuals), suggesting that random errors from one experiment to the next is not a dominant error mechanism.

dual-tone time-dependent pulses with detuning [74]. Additionally, optimization using quantum control techniques is promising for increasing the speed and fidelity of qutrit and qudit operations [59, 64]. Refs. [2, 18] have used phase-modulated signals for quantum control in ^{133}Cs using $d = 7$ and $d = 16$. Using two fully independent transitions A, B with their own modulations may lead to faster and more efficient optimized gates.

Looking forward, the two-qutrit operations necessary for universal quantum information processing [46, 48, 78] will expand the scope of these initial demonstrations, whether in ensembles [26] or single-atom arrays [35]. Opportunities in broader areas, such as for holonomic computing [21, 28, 80, 82, 84] will also take benefit from a comprehensive control over the multilevel state systems developed for qutrit and qudits. While there is increasing potential for neutral atoms to serve in these roles, the general techniques for quantum state control over qudits apply across platforms, and developments across fields will rapidly accelerate this capabilities for all systems.

4.8 Supplementary Material

4.8.1 Operator Derivations

Here we provide details of the the operators necessary for the SU(3) decompositions $\hat{U}^{\mathrm{I}}$ and $\hat{U}^{\mathrm{II}}$.

Derivation of Coupling Operators

The coupling operators $\hat{U}_{\mathrm{A}}$, $\hat{U}_{\mathrm{B}}$, and $\hat{U}_{\mathrm{AB}}$ are produced by driving resonant microwave couplings between states $\{|0\rangle, |1\rangle\}$ and $\{|1\rangle, |2\rangle\}$, as shown in Fig. 4.2(a). In general, when such a resonant dual-tone field is applied to a three-level system, the lab-frame Hamiltonian in the basis $\{|0\rangle, |1\rangle, |2\rangle\}^T$ is

$$\hat{H} = \hbar \begin{pmatrix} \omega_A & |\Omega_A| \sin(\omega_A t + \phi_A) & 0 \\ |\Omega_A| \sin(\omega_A t + \phi_A) & 0 & |\Omega_B| \sin(\omega_B t + \phi_B) \\ 0 & |\Omega_B| \sin(\omega_B t + \phi_B) & \omega_B \end{pmatrix}, \tag{4.10}$$

where ω_{X}, ϕ_{X} and Ω_{X} are the resonant frequency, phase, and Rabi frequency for the transition $\mathrm{X} \in \{A, B\}$ shown in Fig. 4.1. A useful rotating frame for

this analysis is generated by the rotation

$$\hat{W} = \begin{pmatrix} e^{i\omega_A t} & 0 & 0 \\ 0 & 1 & 0 \\ 0 & 0 & e^{i\omega_B t} \end{pmatrix}. \tag{4.11}$$

After transforming the Hamiltonian into this frame $\hat{\tilde{H}} = \hat{W}^\dagger \hat{H} \hat{W} + i\hbar(\partial_t \hat{W})\hat{W}^\dagger$ and applying the rotating wave approximation, the new effective Hamiltonian is

$$\hat{\tilde{H}} = \frac{i\hbar}{2} \begin{pmatrix} 0 & -\Omega_A & 0 \\ \Omega_A^* & 0 & \Omega_B^* \\ 0 & -\Omega_B & 0 \end{pmatrix}. \tag{4.12}$$

where $\Omega_X = |\Omega_X| e^{i\phi_X}$ is the complex coupling parameter. A single-qutrit gate operation performed by applying this Hamiltonian for some duration t is

$$\hat{U} = \exp(-i\hat{\tilde{H}}t/\hbar). \tag{4.13}$$

As one ingredient in our decomposition, we consider SU(2) coupling gates realized by applying a single tone field. If, for example, we impose the condition $\Omega_B = 0$ to eq. (4.12) before using this Hamiltonian to calculate the evolution (4.13) for some duration $t_A = 2\chi_A/|\Omega_A|$, we find a gate operating only on the $|0\rangle \leftrightarrow |1\rangle$ subspace

$$\hat{U}_A(\chi_A, \phi_A) = \begin{pmatrix} \cos\chi_A & -e^{i\phi_A}\sin\chi_A & 0 \\ e^{-i\phi_A}\sin\chi_A & \cos\chi_A & 0 \\ 0 & 0 & 1 \end{pmatrix}, \tag{4.14}$$

which provides amplitude and phase control for the targeted coupling between $|0\rangle \leftrightarrow |1\rangle$. Similarly, for the condition $\Omega_A = 0$ and duration $t_B = 2\chi_B/|\Omega_B|$, we have

$$\hat{U}_{\mathrm{B}}(\chi_B, \phi_B) = \begin{pmatrix} 1 & 0 & 0 \\ 0 & \cos\chi_B & e^{-i\phi_B}\sin\chi_B \\ 0 & -e^{i\phi_B}\sin\chi_B & \cos\chi_B \end{pmatrix} \tag{4.15}$$

which achieves the same for for the targeted coupling between $|1\rangle \leftrightarrow |2\rangle$.

To implement $\hat{U}_{AB}$, both coupling terms in (4.12) are generally non-zero. If we restrict the pulse duration to $t_{\mathrm{AB}} = 2\pi/\sqrt{|\Omega_{\mathrm{A}}|^2 + |\Omega_{\mathrm{B}}|^2}$ as was first

explained in Ref. [41], we find the resonant dual-tone operator first shown in that paper,

$$\hat{U}_{\mathrm{AB}}(\chi_{\mathrm{AB}},\varphi_{\mathrm{AB}}) = \begin{pmatrix} \cos(\frac{\chi_{\mathrm{AB}}}{2}) & 0 & -e^{i\varphi_{\mathrm{AB}}}\sin(\frac{\chi_{\mathrm{AB}}}{2}) \\ 0 & -1 & 0 \\ -e^{-i\varphi_{\mathrm{AB}}}\sin(\frac{\chi_{\mathrm{AB}}}{2}) & 0 & -\cos(\frac{\chi_{\mathrm{AB}}}{2}) \end{pmatrix}, \tag{4.16}$$

where to simplify the expression we have defined $\chi_{\mathrm{AB}} = \arctan|\Omega_{\mathrm{A}}/\Omega_{\mathrm{B}}|$ and $\varphi_{\mathrm{AB}} = \arg(\Omega_{\mathrm{A}}/\Omega_{\mathrm{B}})$. Under this condition for the operator time, the coupling is directly between the states $|0\rangle\leftrightarrow|2\rangle$

In addition to the SU(2) couplings demonstrated here, a diagonal phase gate is required to span SU(3).

Virtual Phase Gates

While Ref. [41] suggests applying far-off resonance fields to perform the phase gate

$$\hat{U}_{\theta}(\eta,\varepsilon) = \exp\begin{pmatrix} i\eta & 0 & 0 \\ 0 & i\varepsilon & 0 \\ 0 & 0 & -i(\eta+\varepsilon) \end{pmatrix}, \tag{4.17}$$

recent qutrit experiments [10, 42, 54, 81] have implemented diagonal phase gates virtually, by manipulating proceeding control fields rather than by manipulating the atoms directly. As they are adjustments to control fields, these virtual phase gates are efficient and have zero duration [52].

Any unitary operators $\hat{U}_a$ that are to be implemented after phase gate $\hat{U}_{\theta}$ are simply phase shifted by the transformation

$$\hat{\tilde{U}}_a = \hat{U}_{\theta}^{\dagger}\hat{U}_a\hat{U}_{\theta}. \tag{4.18}$$

This effectively delays application of the $\hat{U}_{\theta}$ operator until the end of the pulse sequence – notice the location of $\hat{U}_{\theta}$ in the following operator sequence.

$$\begin{aligned} \hat{U}_{\mathrm{gen.}} &= \hat{U}_{a_3}\hat{U}_{a_2}\hat{U}_{a_1}\hat{U}_{\theta}\hat{U}_b \\ &= \hat{U}_{\theta}\hat{U}_{\theta}^{\dagger}\hat{U}_{a_3}\hat{U}_{\theta}\hat{U}_{\theta}^{\dagger}\hat{U}_{a_2}\hat{U}_{\theta}\hat{U}_{\theta}^{\dagger}\hat{U}_{a_1}\hat{U}_{\theta}\hat{U}_b \\ &= \hat{U}_{\theta}\hat{\tilde{U}}_{a_3}\hat{\tilde{U}}_{a_2}\hat{\tilde{U}}_{a_1}\hat{U}_b. \end{aligned} \tag{4.19}$$

Several virtual phase gates are easily combined by tracking the accumulated η and ε through the operator sequence.

The remaining final $\hat{U}_\theta$ operator never needs to be applied because after the last coupling operator (including tomography pulses), the state is projected via $\left|\langle n|\hat{U}_{\text{gen.}}|\psi\rangle\right|^2$, and the phase information is destroyed.

In our experiment, the read-out operators $\hat{R}_i$ are applied after the diagonal phase gate $\hat{U}_\theta$, so these pulses are phase shifted in practice, and modified pulses $\hat{\tilde{R}}_i$ are generated:

$$\hat{\tilde{R}}_{1,2}(\phi) = \hat{R}_{1,2}(\phi + \varepsilon - \eta), \tag{4.20}$$

$$\hat{\tilde{R}}_{3,4}(\phi) = \hat{R}_{3,4}(\phi - \eta - 2\varepsilon), \tag{4.21}$$

$$\hat{\tilde{R}}_{5,6}(\phi) = \hat{R}_{5,6}(\phi - \varepsilon - 2\eta). \tag{4.22}$$

4.8.2 Fourier Transform

The Fourier transform $\hat{F}$ does not have determinant 1, i.e. it is not a member of the group SU(3), however, $i\hat{F}$ is in the group, so the operation can be achieved up to a global phase. The decomposition $\hat{F}^{\text{I}}$ differs from (4.3) by the change of basis $|1\rangle \leftrightarrow |2\rangle$, and the decomposition $\hat{F}^{\text{II}}$ differs from (4.3) by the change of basis $|0\rangle \leftrightarrow |1\rangle$.

4.8.3 Decomposition of Operators

The supplementary material of Ref. [42] shows an algorithm for decomposition of any arbitrary qutrit gate $\hat{U}_{\text{gen.}}$ into SU(2) steps using two single-tone couplings. We show a version of the procedure that works for either single or dual-tone decompositions here for clarity and because we suspect that exposition has typographical errors. A SU(2) coupling on the basis $\{|\, m\,\rangle, |\, n\,\rangle\}$ of area χ and phase ϕ can be expressed as

$$R^{mn}(\chi, \phi) = \exp\left\{-i\frac{\chi}{2}\left[\cos(\phi)\sigma_x^{mn} + \sin(\phi)\sigma_y^{mn}\right]\right\} \tag{4.23}$$

where $\sigma_x^{mn} = |m\rangle\langle n| + |n\rangle\langle m|$ and $\sigma_y^{mn} = i|n\rangle\langle m| - i|m\rangle\langle n|$. Each step of the rotation has

$$\chi = 2\arcsin\sqrt{\frac{|\langle a|\hat{U}_k|m\rangle|^2}{|\langle a|\hat{U}_k|m\rangle|^2 + |\langle a|\hat{U}_k|n\rangle|^2}} \tag{4.24}$$

Table 4.4: Parameters for Operator Decomposition

Decomposition	Step, k	$\hat{U}_k$	a	Coupling basis $\{\|m\rangle, \|n\rangle\}$
$\hat{U}^{\mathrm{I}} = \hat{U}_\theta \hat{U}_A \hat{U}_B \hat{U}_A$	1	$\hat{U}_{\text{gen.}}$	$\|2\rangle$	A: $\{\|0\rangle, \|1\rangle\}$
	2	$\hat{U}_{\text{gen.}} \hat{U}_1^\dagger$	$\|2\rangle$	B: $\{\|1\rangle, \|2\rangle\}$
	3	$\hat{U}_{\text{gen.}} \hat{U}_1^\dagger \hat{U}_2^\dagger$	$\|1\rangle$	A: $\{\|0\rangle, \|1\rangle\}$
$\hat{U}^{\mathrm{II}} = \hat{U}_\theta \hat{U}_A \hat{U}_B \hat{U}_{AB}$	1	$\hat{U}_{\text{gen.}}$	$\|2\rangle$	AB: $\{\|0\rangle, \|2\rangle\}$
	2	$\hat{U}_{\text{gen.}} \hat{U}_1^\dagger$	$\|2\rangle$	B: $\{\|1\rangle, \|2\rangle\}$
	3	$\hat{U}_{\text{gen.}} \hat{U}_1^\dagger \hat{U}_2^\dagger$	$\|1\rangle$	A: $\{\|0\rangle, \|1\rangle\}$

and

$$\phi = \frac{\pi}{2} + \arg\left(\langle a|\hat{U}_k|m\rangle\right) - \arg\left(\langle a|\hat{U}_k|n\rangle\right) \tag{4.25}$$

where $\langle a|\hat{U}_k|m\rangle$ is a matrix element of $\hat{U}_k$ to be zeroed and $\hat{U}_k$ is the remaining remaining portion of $\hat{U}_{\text{gen.}}$ to be implemented. The values of $|a\rangle$, $|m\rangle$, $|n\rangle$, and $\hat{U}_k$ to be used for each step of the decomposition are given in Table 4.4, and a Python implementation of the general decomposition is provided in listing **??**.

4.8.4 Signal Generation

To generate microwave signals with arbitrary phase, frequency, and amplitude control, we mix the output of an arbitrary waveform generator with a microwave signal. The microwave signal is detuned 100 MHz below the hyperfine splitting of ^{87}Rb, and is produced by a BNC Model 845 Microwave Signal Generator. A Tektronix AWG5204 controlled by Python software produces signals at 5 GS/s which are pre-amplified before being combined with the microwave-frequency signal in a double-balanced mixer. The mixed signal is amplified by a 25 W microwave amplifier before being directed towards the atoms through a waveguide. Higher Rabi frequencies would certainly be achievable with higher microwave power or a more focused beam.

4.8.5 Error Mechanisms

In this section we discuss and evaluate some mechanisms in our system that could cause the fidelity and purity errors from table 4.3 in the main text. We

note that dephasing is not a leading source of error, as our T_2^* times are well over 1 ms.

Detuning

When performing manipulations using our apparatus, we frequently find readjusting magnetic field biases necessary to keep the two generated frequencies resonant with the atomic frequencies ω_A and ω_B. This field instability of order 30 minutes is a limitation of our system, and not a limitation of neutral atom computation in general. Because of concerns about the continued resonance of operations, in addition to frequent checks of the biases we average final populations for tomographic tests as discussed in the main text.

We numerically simulate the operations $\hat{F}^{\mathrm{I}}$ and $\hat{F}^{\mathrm{II}}$, adding detuning deliberately,

$$\hat{H}_{\mathrm{detun.}} = \hbar \begin{pmatrix} \omega_A & \mathcal{O}_A & 0 \\ \mathcal{O}_A & 0 & \mathcal{O}_B \\ 0 & \mathcal{O}_B & \omega_B \end{pmatrix} \tag{4.26}$$

where we have defined $\mathcal{O}_X = |\Omega_X| \sin\left[(\omega_X + \Delta_X)t + \phi_X\right]$. Moving into the rotating frame,

$$\hat{\tilde{H}}_{\mathrm{detun.}} = \frac{i\hbar}{2} \begin{pmatrix} 0 & -\Omega_A e^{i\Delta_A t} & 0 \\ (\Omega_A e^{i\Delta_A t})^* & 0 & (\Omega_B e^{i\Delta_B t})^* \\ 0 & -\Omega_B e^{i\Delta_B t} & 0 \end{pmatrix}, \tag{4.27}$$

and, setting $\Delta = \Delta_A = -\Delta_B$ for each of the decomposed SU(2) steps, we generate the curves of figure 4.5. If detuning applied equally to all atoms in the ensemble was a strong error mechanism in our system, we would expect to see lower $\mathcal{F}$ for the dual-tone $\hat{F}^{\mathrm{II}}$ than the single-tone $\hat{F}^{\mathrm{I}}$, and we would not expect to see a drop in $\mathcal{P}$. In our experiment, the fidelity for both decompositions is of a similar magnitude, and we observe a significant drop in $\mathcal{P}$, so this detuning model does not explain the main error mechanism present.

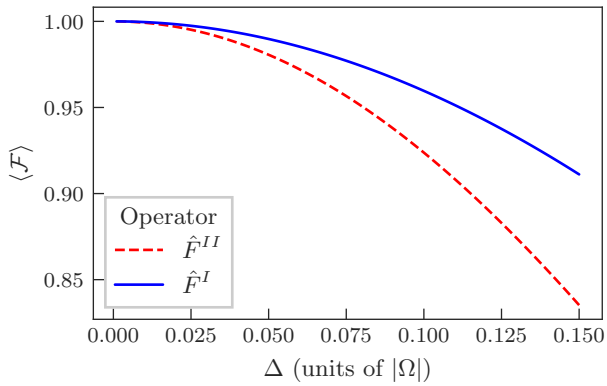

Figure 4.5: Simulated effect of detuning on the final fidelity measurement, averaged across the states $|0\rangle$, $|1\rangle$, and $|2\rangle$, where $\Omega^2 = |\Omega_A|^2 + |\Omega_B|^2$.

Stark Shifts Caused by the Optical Dipole Trap

During the application of microwave pulses for state manipulation, the atomic ensemble is held in a two-beam crossed optical dipole trap. This laser with approximately 0.4 W of power holds atoms in place by creating a 3D Gaussian trap with depth 6 µK. The potential experienced by the Bose-Einstein condensed atoms near its centre is approximated by a spherically symmetric harmonic oscillator with trap frequency $\omega_{\text{ho}} \approx 2\pi \times 100\,\text{Hz}$. The 10^5 atoms are held within a Thomas-Fermi radius $R_{\text{TF}} = 6.5\,\mu\text{m}$.

In a hyperfine manifold, we expect Stark shifts to take the form [3, 70]

$$E_{\text{S}} = -\frac{1}{2}\alpha_0 \mathcal{E}^2 - \frac{1}{2}\alpha_2^F \mathcal{E}^2 \left[\frac{3m_F^2 - F(F+1)}{F(2F-1)}\right], \tag{4.28}$$

where α_0 is the scalar polarizability of the ground state, α_2^F is the tensor polarizability for hyperfine level F, m_F is the Zeeman sub-level, and $\mathcal{E}$ is the electric field strength.

The scalar Stark shift will perturb the energy of both the $|F = 1\rangle$ manifold and the $|F = 2\rangle$ manifold equally. As a result, regardless of the position of the atoms in the trap, all atoms will simultaneously be resonant. At the centre of the cloud, both levels are shifted by about $h \times 6.0\,\text{kHz}$. At R_{TF} from the centre, the shift is about $h \times 5.9\,\text{kHz}$, a difference of about $h \times 100\,\text{Hz}$.

The tensor Stark shift perturbs the energy of the $|F = 1, m_F = 1\rangle = |1\rangle$ state without having an effect on $|F = 2\rangle$ states. As a result, atoms in the

Table 4.5: Simulated reduction in fidelity, purirty, and purity-adjusted fidelity due to trap-induced Stark shifts.

Operator	State	$\mathcal{P}$	$\mathcal{F}$	$\mathcal{F}_{\text{pure}}$
$\hat{F}^{II}$	$\|0\rangle$	0.953	0.980	1.009
	$\|1\rangle$	0.950	0.974	1.008
	$\|2\rangle$	0.953	0.980	1.009
$\hat{F}^{I}$	$\|0\rangle$	0.963	0.981	1.006
	$\|1\rangle$	0.965	0.986	1.007
	$\|2\rangle$	0.965	0.986	1.007

centre of the trap will have different resonant frequencies for both transitions ω_A and ω_B from atoms at the two ends of the trap. The magnitude of the tensor shift for $|1\rangle$ is $h \times 25.8\,\text{kHz}$ at the centre of the trap and $h \times 25.3\,\text{kHz}$ at R_{TF}. The probability distribution function is [20],

$$\begin{aligned} n_{1\text{D}}(r) &= \int_{4\pi} r^2 d\Omega\, n_{3\text{D}}(\mathbf{r}) \\ &= \int_{4\pi} r^2 d\Omega \frac{\mu}{g}\left(1 - \frac{r^2}{R_{\text{TF}}^2}\right) \\ &= \frac{4\pi\mu r^2}{g}\left(1 - \frac{r^2}{R_{\text{TF}}^2}\right) \end{aligned} \tag{4.29}$$

where r is the radial coordinate, m_{Rb} is the mass of an ^{87}Rb atom, $\mu = m_{\text{Rb}}\omega_{ho}^2 R_{\text{TF}}^2/2$ is the chemical potential, and $g = 4\pi\hbar^2 a/m_{\text{Rb}}$ is the coupling constant. We can obtain the mean Stark shift,

$$\langle E_{\text{S}}\rangle = \int dr\, n_{1\text{D}}(r) E_{\text{S}}(r), \tag{4.30}$$

and assuming our frequency calibration is accurate to this mean, the detuning,

$$\Delta(r) = E_{\text{S}}(r) - \langle E_{\text{S}}\rangle. \tag{4.31}$$

To evaluate the purity and fidelity decay caused by the tensor Stark shift, we sample 1000 detunings from $\Delta(r)$, weight them by $n_{1\text{D}}(r)$, and calculate the $\hat{\rho}_{\text{out}}$ found by tomography from this distribution comparing it to the $\hat{\rho}$ for Stark-shift-free evolution. The results are shown in table 4.5.

We also perform the same purity recovery algorithm from (4.9), with results shown in the table. As expected, the purity recovery algorithm results in a perfect fidelity. We conclude that it is plausible that the relatively low purity and some of the error in $\mathcal{F}$ we find in the main results (table 4.3) may be caused by Stark shifts from the optical dipole trap.

Calibration

For a high fidelity operator, the many control pulses used in our experiment including $\hat{U}_{\text{prep.}}$, $\hat{U}_A$, $\hat{U}_B$, $\hat{U}_{AB}$, and $\hat{R}_i$ must simultaneously have their pulse durations calibrated accurately and the detuning for both tones must be negligible (less than $0.025|\Omega| \approx 2\pi \times 50\,\text{Hz}$ as suggested by figure 4.5).

To find the resonant frequencies, the duration and frequency of the two tones were adjusted manually until 100 % of the atomic population was transferred between the states. The duration of each operator was also calibrated manually by starting from each computational basis state and scanning the operator duration to finding the point where the population transfer matches theory.

In the ideal case, we would assume Ω is constant during the application of an operator, and we could determine the Rabi frequency to high precision by performing long pulses $\chi = n\pi$. In our system, long pulses would not be a good calibration technique because the Rabi frequency Ω is not constant over longer time periods. This may be a limitation of our microwave amplifier or magnetic field bias stability. To account for this effect, each pulse duration was calibrated individually for its position in the pulse sequence, and only short pulses were used in the experiment.

Our current microwave system is not optimized for high Rabi frequencies. A rectangular waveguide is aimed towards the atoms from a distance of approximately 15 cm before the microwaves are allowed to propagate through free space. The microwaves which impinge on the atoms are sent off-axis and do not demonstrate any significant degree of polarization, driving σ^+, σ^- and π transitions. Work is underway to improve this system significantly by using

a helical antenna to generate well-defined $\sigma^{\pm}$ polarizations based on the work of Ref. [83].

Chapter 5

Conclusion

This work has demonstrated a single-qutrit gate, the quantum Fourier transform, on an ensemble of ^{87}Rb. This gate was decomposed into SU(2) rotations in two ways, one of which required a rotation between levels of the qutrit without an easily controllable coupling. Rotation on that coupling was synthesized by sending a resonant dual-tone operator. Both decompositions produced similar final state fidelities, showing that the dual-tone operator had similar performance to a conventional resonant gate. This was the first experimental demonstration of the resonant dual-tone operator, and the first qutrit demonstration in ultracold atoms.

The control mechanisms demonstrated here on an ensemble of atoms are quite general. For any three-state subset of a controllable quantum system, if two couplings are more easily addressable than the other, then driving the two preferred couplings can effectively mediate a transition as though they formed the third.

Inhomogeneity in the optical dipole trap which holds the atoms appears to be the most significant error source. This causes atoms near the edge of the trap to evolve out of phase with those in its center, which gives the ensemble qubit a badly-defined phase and thus a loss of purity.

5.1 Project Extensions

This section discusses possible extensions to the qutrit project.

- Continuing with only one qutrit, this project could be extended to look at more sophisticated, optimized pulse shapes. For example, Vitanov [74] shows that decomposing gates by quantum Householder reflections scales much better with qudit dimension than two-level unitary rotations. A decomposition of this type could be tested on the *Quantum Simulation* system. This would require a good calibration of the Rabi frequencies, which is a challenge with the current microwave system.

- More powerful magnetic field biases could be used to deliberately induce a significant quadratic Zeeman term, which would fully separate the control frequencies for each of the microwave resonances. This could be used for fully RF control of a qutrit in the $F = 1$ hyperfine manifold, or for controlling up to all 8 of the hyperfine states, which would yield a Hilbert space equivalent to 3 qubits.

- The *Quantum Simulation* system is limited to only one ensemble cloud of qutrits. The natural extension into a multi-qutrit system would require a new system. While multi-qutrit gates on atomic ensembles could be achieved [26, 68], switching to single-atom qutrits in a lattice would likely be a more effective approach. These single-atom qutrits could use the same two-qudit gates developed for qubits. For example, a desired gate between states $|2\rangle \otimes |2\rangle$ and $|0\rangle \otimes |0\rangle$ could be achieved by a coupling between $|1\rangle \otimes |1\rangle$ and $|0\rangle \otimes |0\rangle$ preceeded and proceeded by π gates on the B coulings.

5.2 The Future of Quantum Computing

It is an exciting time in the field of quantum computing. Meaningful research is being carried out by groups across academia and industry. Currently, almost all of that research is based on qubits. In principle, a switch from qubits to qutrits or higher-dimensional qudits on many leading architectures would be simple. Making that change would reduce the required number of qudits to reach a desired Hilbert space size, and could reduce the number of two-qudit

gates, leading to higher overall system fidelities. Alternatively, an existing system could access a larger Hilbert space by switching to from qubits to qutrits. For example, converting an eight qubit system into an eight qutrit system would expand the accessible Hilbert space by a factor of 25.

The vision of an error-corrected quantum processor is still far from reality, but there is a lot of interesting work to be found along the way. I hope that we continue to see rapid development and sustained interest in pushing the field forward from private industry, academia, government agencies, and of course from enthusiastic graduate students.

References

[1] A. Abragam, "The adiabatic theorem, adiabatic passage", in *The principles of nuclear magnetism* (Clarendon Press, 1961), pp. 34–36.

[2] B. E. Anderson, H. Sosa-Martinez, C. A. Riofrío, I. H. Deutsch, and P. S. Jessen, "Accurate and Robust Unitary Transformations of a High-Dimensional Quantum System", Physical Review Letters **114**, 240401 (2015).

[3] M. Auzinsh, D. Budker, and S. Rochester, *Optically polarized atoms* (Oxford University Press, London, England, Aug. 2010).

[4] A. Babazadeh, M. Erhard, F. Wang, M. Malik, R. Nouroozi, M. Krenn, and A. Zeilinger, "High-Dimensional Single-Photon Quantum Gates: Concepts and Experiments", Physical Review Letters **119**, 180510 (2017).

[5] T. Bækkegaard, L. B. Kristensen, N. J. S. Loft, C. K. Andersen, D. Petrosyan, and N. T. Zinner, "Realization of efficient quantum gates with a superconducting qubit-qutrit circuit", Scientific Reports **9**, 13389 (2019).

[6] S. D. Barrett, P. P. Rohde, and T. M. Stace, "Scalable quantum computing with atomic ensembles", New J. Phys. **12**, 093032 (2010).

[7] S. Bartolucci, P. Birchall, H. Bombín, H. Cable, C. Dawson, M. Gimeno-Segovia, E. Johnston, K. Kieling, N. Nickerson, M. Pant, F. Pastawski, T. Rudolph, and C. Sparrow, "Fusion-based quantum computation", Nature Communications **14** (2023) 10.1038/s41467-023-36493-1.

[8] J.-L. Basdevant, *Lectures on quantum mechanics*, 2nd ed. (Springer, 2016).

[9] R. Bianchetti, S. Filipp, M. Baur, J. M. Fink, C. Lang, L. Steffen, M. Boissonneault, A. Blais, and A. Wallraff, "Control and tomography of a three level superconducting artificial atom", Phys. Rev. Lett. **105**, 223601 (2010).

[10] M. S. Blok, V. V. Ramasesh, T. Schuster, K. O'Brien, J. M. Kreikebaum, D. Dahlen, A. Morvan, B. Yoshida, N. Y. Yao, and I. Siddiqi, "Quantum Information Scrambling on a Superconducting Qutrit Processor", Phys. Rev. X **11**, 21010 (2021).

[11] D. Bluvstein, H. Levine, G. Semeghini, T. T. Wang, S. Ebadi, M. Kalinowski, A. Keesling, N. Maskara, H. Pichler, M. Greiner, V. Vuletić, and M. D. Lukin, "A quantum processor based on coherent transport of entangled atom arrays", Nature **604**, 451–456 (2022).

[12]A. Bocharov, M. Roetteler, and K. M. Svore, "Factoring with qutrits: Shor's algorithm on ternary and metaplectic quantum architectures", Physical Review A **96**, 012306 (2017).

[13]Y. I. Bogdanov, M. V. Chekhova, S. P. Kulik, G. A. Maslennikov, A. A. Zhukov., C. H. Oh, and M. K. Tey, "Qutrit State Engineering with Biphotons", Physical Review Letters **93**, 230503 (2004).

[14]D. Bruß and C. Macchiavello, "Optimal Eavesdropping in Cryptography with Three-Dimensional Quantum States", Physical Review Letters **88**, 127901 (2002).

[15]C. D. Bruzewicz, J. Chiaverini, R. McConnell, and J. M. Sage, "Trapped-ion quantum computing: Progress and challenges", Applied Physics Reviews **6** (2019) 10.1063/1.5088164.

[16]Y. Cao, J. Romero, and A. Aspuru-Guzik, "Potential of quantum computing for drug discovery", IBM Journal of Research and Development **62**, 6:1–6:20 (2018).

[17]C. M. Caves and G. J. Milburn, "Qutrit entanglement", Opt. Commun. **179**, 439–446 (2000).

[18]S. Chaudhury, S. Merkel, T. Herr, A. Silberfarb, I. H. Deutsch, and P. S. Jessen, "Quantum Control of the Hyperfine Spin of a Cs Atom Ensemble", Physical Review Letters **99**, 163002 (2007).

[19]Z. Chen, J. D. Murphree, and N. P. Bigelow, "SU(2) geometric phase induced by a periodically driven Raman process in an ultracold dilute Bose gas", Physical Review A **101**, 013606 (2020).

[20]F. Dalfovo, S. Giorgini, L. P. Pitaevskii, and S. Stringari, "Theory of bose-einstein condensation in trapped gases", Rev. Mod. Phys. **71**, 463–512 (1999).

[21]S. Danilin, A. Vepsäläinen, and G. S. Paraoanu, "Experimental state control by fast non-Abelian holonomic gates with a superconducting qutrit", Physica Scripta **93**, 055101 (2018).

[22]S. Debnath, N. M. Linke, C. Figgatt, K. A. Landsman, K. Wright, and C. Monroe, "Demonstration of a small programmable quantum computer with atomic qubits", Nature **536**, 63–66 (2016).

[23]C. L. Degen, F. Reinhard, and P. Cappellaro, "Quantum sensing", Reviews of Modern Physics **89**, 1–39 (2017).

[24]D. P. DiVincenzo, "The physical implementation of quantum computation", Fortschritte der Physik **48**, 771–783 (2000).

[25]S. Dogra, Arvind, and K. Dorai, "Determining the parity of a permutation using an experimental NMR qutrit", Phys. Lett. A **378**, 3452–3456 (2014).

[26]M. Ebert, M. Kwon, T. G. Walker, and M. Saffman, "Coherence and Rydberg Blockade of Atomic Ensemble Qubits", Phys. Rev. Lett. **115**, 093601 (2015).

[27]"Experimental quantum cryptography with qutrits", New Journal of Physics **8**, 75–75 (2006).

[28]G. Feng, G. Xu, and G. Long, "Experimental Realization of Nonadiabatic Holonomic Quantum Computation", Physical Review Letters **110**, 190501 (2013).

[29]C. J. Foot, *Atomic physics*, Vol. 7 (OUP Oxford, 2004).

[30]A. G. Fowler, A. M. Stephens, and P. Groszkowski, "High-threshold universal quantum computation on the surface code", Physical Review A - Atomic, Molecular, and Optical Physics **80**, 1–14 (2009).

[31]S. Ganesh, "Modelling spin-1 87rb bose einstein condensate to study ground states under inhomogenous magnetic fields", MA thesis (KTH Royal Institute of Technology, 2019).

[32]Z. Gedik, I. A. Silva, B. Çakmak, G. Karpat, E. L. Vidoto, D. O. Soares-Pinto, E. R. DeAzevedo, and F. F. Fanchini, "Computational speed-up with a single qudit", Sci. Rep. **5**, 14671 (2015).

[33]N. Gisin, G. Ribordy, W. Tittel, and H. Zbinden, "Quantum cryptography", Reviews of Modern Physics **74**, 145–195 (2002).

[34]P. Gokhale, J. M. Baker, C. Duckering, F. T. Chong, N. C. Brown, and K. R. Brown, "Extending the Frontier of Quantum Computers with Qutrits", IEEE Micro **40**, 64–72 (2020).

[35]L. Henriet, L. Beguin, A. Signoles, T. Lahaye, A. Browaeys, G.-O. Reymond, and C. Jurczak, "Quantum computing with neutral atoms", Quantum **4**, 327 (2020).

[36]A. Ho, J. McClean, and S. P. Ong, "The Promise and Challenges of Quantum Computing for Energy Storage", Joule **2**, 810–813 (2018).

[37]T. Hrushevskyi, "Quantum gas apparatus for Bose-Einstein condensation of 87 Rb", MA thesis (University of Alberta, 2017).

[38]S. S. Ivanov, H. S. Tonchev, and N. V. Vitanov, "Time-efficient implementation of quantum search with qudits", Physical Review A **85**, 062321 (2012).

[39]R. Jozsa, "Fidelity for mixed quantum states", J. Mod. Opt. **41**, 2315–2323 (1994).

[40]Y. Kawashima, E. Lloyd, M. P. Coons, Y. Nam, S. Matsuura, A. J. Garza, S. Johri, L. Huntington, V. Senicourt, A. O. Maksymov, J. H. Nguyen, J. Kim, N. Alidoust, A. Zaribafiyan, and T. Yamazaki, "Optimizing electronic structure simulations on a trapped-ion quantum computer using problem decomposition", Communications Physics **4**, 1–9 (2021).

[41]A. B. Klimov, R. Guzmán, J. C. Retamal, and C. Saavedra, "Qutrit quantum computer with trapped ions", Phys. Rev. A **67**, 7 (2003).

[42]M. Kononenko, M. A. Yurtalan, S. Ren, J. Shi, S. Ashhab, and A. Lupascu, "Characterization of control in a superconducting qutrit using randomized benchmarking", Phys. Rev. Research **3**, L1042007 (2021).

[43]B. P. Lanyon, T. J. Weinhold, N. K. Langford, J. L. O'Brien, K. J. Resch, A. Gilchrist, and A. G. White, "Manipulating biphotonic qutrits", Physical Review Letters **100** (2008) 10.1103/physrevlett.100.060504.

[44]B. P. Lanyon, M. Barbieri, M. P. Almeida, T. Jennewein, T. C. Ralph, K. J. Resch, G. J. Pryde, J. L. O'Brien, A. Gilchrist, and A. G. White, "Simplifying quantum logic using higher-dimensional Hilbert spaces", Nature Physics **5**, 134–140 (2009).

[45]J. Lindon, A. Tashchilina, L. W. Cooke, and L. J. LeBlanc, "Complete unitary qutrit control in ultracold atoms", Phys. Rev. Appl. **19**, 034089 (2023).

[46]P. J. Low, B. M. White, A. A. Cox, M. L. Day, and C. Senko, "Practical trapped-ion protocols for universal qudit-based quantum computing", Physical Review Research **2**, 033128 (2020).

[47]H. Lu, Z. Hu, M. S. Alshaykh, A. J. Moore, Y. Wang, P. Imany, A. M. Weiner, and S. Kais, "Quantum Phase Estimation with Time-Frequency Qudits in a Single Photon", Advanced Quantum Technologies **3**, 1900074 (2020).

[48]M. Luo and X. Wang, "Universal quantum computation with qudits", Science China Physics, Mechanics & Astronomy **57**, 1712–1717 (2014).

[49]A. I. Lvovsky, "Iterative maximum-likelihood reconstruction in quantum homodyne tomography", J. Opt. B **6**, S565 (2004).

[50]L. S. Madsen, F. Laudenbach, M. F. Askarani, F. Rortais, T. Vincent, J. F. F. Bulmer, F. M. Miatto, L. Neuhaus, L. G. Helt, M. J. Collins, A. E. Lita, T. Gerrits, S. W. Nam, V. D. Vaidya, M. Menotti, I. Dhand, Z. Vernon, N. Quesada, and J. Lavoie, "Quantum computational advantage with a programmable photonic processor", Nature **606**, 75–81 (2022).

[51]D. Mc Hugh and J. Twamley, "Trapped-ion qutrit spin molecule quantum computer", New J. Phys. **7**, 174 (2005).

[52]D. C. McKay, C. J. Wood, S. Sheldon, J. M. Chow, and J. M. Gambetta, "Efficient Z gates for quantum computing", Phys. Rev. A **96**, 022330 (2017).

[53]G. Molina-Terriza, A. Vaziri, R. Ursin, and A. Zeilinger, "Experimental quantum coin tossing", Phys. Rev. Lett. **94**, 040501 (2005).

[54]A. Morvan, V. V. Ramasesh, M. S. Blok, J. M. Kreikebaum, K. O'Brien, L. Chen, B. K. Mitchell, R. K. Naik, D. I. Santiago, and I. Siddiqi, "Qutrit Randomized Benchmarking", Phys. Rev. Lett. **126**, 210504 (2021).

[55]National Centers for Environmental Information, *World Magnetic Model Mangetic Field Calculator*, (2023) https://www.ngdc.noaa.gov/geomag/calculators/magcalc.shtml#igrfwmm.

[56]V. Novičenko and G. Juzeliūnas, "Non-Abelian geometric phases in periodically driven systems", Physical Review A **100**, 012127 (2019).

[57]M. A. Nuelsen and I. L. Chuang, *Quantum computation and quantum information*, 10th anniversary (Cambridge University Press, Cambridge, UK, 2010).

[58]S. Olmschenk, R. Chicireanu, K. D. Nelson, and J. V. Porto, "Randomized benchmarking of atomic qubits in an optical lattice", New J. Phys. **12**, 113007 (2010).

[59]S. Omanakuttan, A. Mitra, M. J. Martin, and I. H. Deutsch, "Quantum optimal control of ten-level nuclear spin qudits in 87Sr", Physical Review A **104**, L060401 (2021).

[60]R. Orús, S. Mugel, and E. Lizaso, "Quantum computing for finance: Overview and prospects", Reviews in Physics **4** (2019) 10.1016/j.revip.2019.100028.

[61]I. Othmani, M. LaDue, and M. Mevissen, *Exploring quantum computing use cases for logistics*, tech. rep. (IBM Institute for Business Value, 2022).

[62]J. M. Pino, J. M. Dreiling, C. Figgatt, J. P. Gaebler, S. A. Moses, M. S. Allman, C. H. Baldwin, M. Foss-Feig, D. Hayes, K. Mayer, C. Ryan-Anderson, and B. Neyenhuis, "Demonstration of the trapped-ion quantum CCD computer architecture", Nature **592**, 209–213 (2021).

[63]Qiskit Team, *Qiskit Textbook*, 2022.

[64]J. Randall, A. M. Lawrence, S. C. Webster, S. Weidt, N. V. Vitanov, and W. K. Hensinger, "Generation of high-fidelity quantum control methods for multilevel systems", Physical Review A **98**, 043414 (2018).

[65]J. Randall, S. Weidt, E. D. Standing, K. Lake, S. C. Webster, D. F. Murgia, T. Navickas, K. Roth, and W. K. Hensinger, "Efficient preparation and detection of microwave dressed-state qubits and qutrits with trapped ions", Physical Review A **91**, 012322 (2015).

[66]M. Reiher, N. Wiebe, K. M. Svore, D. Wecker, and M. Troyer, "Elucidating reaction mechanisms on quantum computers", Proceedings of the National Academy of Sciences of the United States of America **114**, 7555–7560 (2017).

[67]M. Ringbauer, M. Meth, L. Postler, R. Stricker, R. Blatt, P. Schindler, and T. Monz, "A universal qudit quantum processor with trapped ions", 2021.

[68]M. Saffman, "Quantum computing with atomic qubits and Rydberg interactions: progress and challenges", J. Phys. B **49**, 202001 (2016).

[69]C. Schaeff, R. Polster, M. Huber, S. Ramelow, and A. Zeilinger, "Experimental access to higher-dimensional entangled quantum systems using integrated optics", Optica **2**, 523 (2015).

[70]D. A. Steck, *Rubidium 87 D Line Data*, tech. rep. 2 (Self Published, 2010), p. 31.

[71]L.-M. Steinert, P. Osterholz, R. Eberhard, L. Festa, N. Lorenz, Z. Chen, A. Trautmann, and C. Gross, "Spatially programmable spin interactions in neutral atom arrays", arxiv.org, 2206.12385 (2022).

[72]S. Sugawa, F. Salces-Carcoba, Y. Yue, A. Putra, and I. B. Spielman, "Wilson loop and Wilczek-Zee phase from a non-Abelian gauge field", npj Quantum Information **7**, 144 (2021).

[73]R. T. Thew, K. Nemoto, A. G. White, and W. J. Munro, "Qudit quantum-state tomography", Phys. Rev. A **66**, 012303 (2002).

[74]N. V. Vitanov, "Synthesis of arbitrary SU(3) transformations of atomic qutrits", Phys. Rev. A **85**, 032331 (2012).

[75]Y. Wang, A. Kumar, T.-Y. Wu, and D. S. Weiss, "Single-qubit gates based on targeted phase shifts in a 3D neutral atom array", Science **352**, 1562–1565 (2016).

[76]Y. Wang, X. Zhang, T. A. Corcovilos, A. Kumar, and D. S. Weiss, "Coherent Addressing of Individual Neutral Atoms in a 3D Optical Lattice", Physical Review Letters **115**, 043003 (2015).

[77]Y. Wang, S. Crain, C. Fang, B. Zhang, S. Huang, Q. Liang, P. H. Leung, K. R. Brown, and J. Kim, "High-Fidelity Two-Qubit Gates Using a Microelectromechanical-System-Based Beam Steering System for Individual Qubit Addressing", Physical Review Letters **125**, 150505 (2020).

[78]Y. Wang, Z. Hu, B. C. Sanders, and S. Kais, "Qudits and High-Dimensional Quantum Computing", Front. Phys. **8**, 589504 (2020).

[79]J. Wurtz, A. Bylinskii, B. Braverman, J. Amato-Grill, S. H. Cantu, F. Huber, A. Lukin, F. Liu, P. Weinberg, J. Long, S.-T. Wang, N. Gemelke, and A. Keesling, *Aquila: quera's 256-qubit neutral-atom quantum computer*, 2023.

[80]Y. Xu, Z. Hua, T. Chen, X. Pan, X. Li, J. Han, W. Cai, Y. Ma, H. Wang, Y. P. Song, Z.-Y. Xue, and L. Sun, "Experimental Implementation of Universal Nonadiabatic Geometric Quantum Gates in a Superconducting Circuit", Physical Review Letters **124**, 230503 (2020).

[81]M. A. Yurtalan, J. Shi, M. Kononenko, A. Lupascu, and S. Ashhab, "Implementation of a Walsh-Hadamard Gate in a Superconducting Qutrit", Phys. Rev. Lett. **125**, 180504 (2020).

[82]P. Zanardi and M. Rasetti, "Holonomic quantum computation", Physics Letters A **264**, 94–99 (1999).

[83]Y.-G. Zheng, L. Jiang, Z.-H. Zhu, W.-Y. Zhang, Z.-Y. Zhou, B. Xiao, and Z.-S. Yuan, "A compact gain-enhanced microwave helical antenna for 87rb atomic experiments", Review of Scientific Instruments **93** (2022) 10.1063/5.0088161.

[84]B. B. Zhou, P. C. Jerger, V. O. Shkolnikov, F. J. Heremans, G. Burkard, and D. D. Awschalom, "Holonomic Quantum Control by Coherent Optical Excitation in Diamond", Physical Review Letters **119**, 140503 (2017).